PAN-AFRICAN UNIVERSITY

INSTITUTE FOR WATER AND ENERGY SCIENCES

(including CLIMATE CHANGE)

Master Dissertation

Submitted in partial fulfillment of the requirements for the Master degree in
Energy Engineering

Presented By

Chikezie, Williams UGOKWE

IMPROVING THE EFFICIENCY AND REPRODUCIBILITY OF ORGANIC-INORGANIC HALIDE PEROVSKITE SOLAR CELL

Defended on 3rd September, 2018 in the presence of the following Committee

Chair:	Mustapha Benmouna	Prof	University of Tlemcen
Supervisor:	Harald Hoppe	PhD	Friedrich-Schiller-Universität Jena
External Examiner:	Abdellah Benyoucef	PhD	PAUWES
Internal Examiner:	Erick Tambo	PhD	PAUWES

Academic Year: 2017/2018

DECLARATION

I Chikezie Williams Ugokwe, hereby declare that this thesis titled "Improving the Efficiency and Reproducibility of Organic-Inorganic Halide Perovskite Solar Cell" is my original work and that no part of it has been presented for any academic purpose or other purposes that are against the Pan African University ethics and conduct of research in any other time before any University. I also declare that all other works of people cited in this thesis have been duly recognized as required by academic rules and ethics.

....   …….……………...

CHIKEZIE WILLIAMS UGOKWE   **Date**

CERTIFICATION

I hereby certify that this master's thesis by **Chikezie Williams UGOKWE**, an Energy Engineering student of Pan African University Institute of Water and Energy Sciences (including climate change) (PAUWES), Tlemcen, Algeria, was done under my supervision.

…………………………………   …………………………………….
             Supervisor   **Date**

Dr. Harald Hoppe

…………………………………   …………………………….....................

Professor Abdellatif ZERGA   **Date**

Director PAUWES

DEDICATION

In loving memory of Chizoba Henrietta Ugokwe

ACKNOWLEDGMENTS

ABSTRACT

Organic-inorganic halide perovskites have garnered a lot of attention in the field of photovoltaic materials research. This novel PV material possesses a combination of remarkable optoelectronic properties, such as steep optical absorption edge and high absorption coefficients, long charge carrier diffusion lengths and lifetimes. Solution processability, cheap starting materials, and striking optoelectronic properties have these materials a cheaper alternative to the quite expensive widely used polycrystalline silicon for photovoltaic applications.

The focus of this study is on improving efficiency of the inverted planar organic-inorganic halide perovskites based solar cell with glass/ITO/PEDOT:PSS/Perovskite/PCBM/TiOx/Al layers stack. To improve efficiency, a layer by layer approach of optimization was adopted and the effects of each step were also compared as the perovskite synthesis route was varied. Results show that while room temperature methylamine gas treatment improved the crystallinity of MAPI ($CH_3NH_3PbI_{3-x}Cl_x$) perovskite, it converts CsMAFA ($Cs_5(FA_{0.83}MA_{0.17})_{95}Pb(I_{0.83}Br_{0.17})_3$) perovskite to its non-photovoltaic yellow polymorph. We found improved crystal growth for the CsMAFA perovskite is best achieved via DMF solvent vapor annealing. Through PEDOT:PSS and PCBM layers optimization, a maximum PCE of 2.11% and 13.49% were achieved for MAPI and CsMAFA perovskites solar cells respectively.

Keywords: perovskites, thin films, solar cells, crystals, optimization.

RESUME

Les pérovskites aux halogénures organiques-inorganiques ont reçu beaucoup d'attention dans le domaine de recherche des matériaux photovoltaïques. Ce nouveau matériau photovoltaïque possède une combinaison de propriétés optoélectroniques remarquables telles qu'une importante bande d'absorption optique et des coefficients d'absorption élevés, de grande distance de diffusion des porteurs de charge et de durées de vie. Processabilité des solutions, matières premières peu coûteuses, remarquables propriétés optoélectroniques font de ces matériaux une alternative moins chère aux relativement chères et largement utilisés silicones polycristallins pour les applications photovoltaïques.

Cette étude est axée sur l'amélioration de l'efficacité des cellules photovoltaïques inversées basées sur les pérovskites planes à halogénures organique-inorganique avec comme empilement : verre/ITO/PEDOT:PSS/Pérovskite/PCBM/TiOx/Al. Pour améliorer l'efficacité, une approche couche par couche de l'optimisation a été adoptée et les effets de chaque étape ont également été comparées à mesure que la voie de synthèse variait. Les résultats montrent que pendant que le traitement au gaz méthylamine à température ambiante augmente la cristallinité de la pérovskite MAPI ($CH_3NH_3PbI_{3-x}Cl_x$), ce dernier convertit la pérovskite CsMAFA ($Cs_5(FA_{0.83}MA_{0.17})_{95}Pb(I_{0.83}Br_{0.17})_3$) en sa forme polymorphe jaune non-photovoltaïque. Nous avons trouvé que la croissance cristalline améliorée pour la pérovskite CsMAFA est mieux assurée via le recuit aux vapeurs de solvant au DMF. A travers des optimisations des couches de PEDOT :PSS et de PCBM, un PCE maximum de 2,11% et 13,49% ont été atteint pour les pérovskites MAPI et CsMAFA respectivement

Table of Contents

List of Figures

xiii

List of Tables

List of Abbreviation and Symbols

A/s	Angstrom per second
Al	Aluminum
Al_2O_3	Aluminum(III) oxide
AM1.5	Air Mass 1.5, reference solar spectrum
Br	Bromine
Ca	Calcium
$CaTiO_3$	Calcium titanium oxide
CB	Conduction Band
CH_3NH_2	Methylamine
CH_3NH_3Cl	Methylammonium chloride
CH_3NH_3I	Methylammonium iodide
$CH_3NH_3PbI_3$	Methylammonium lead iodide
$CH_3NH_3PbI_{3-x}Cl_x$	Methylammonium lead mixed iodide-chloride
Cl	Chlorine
Cs	Cesium
CsMAFA	Mixed Cation (Cs, MA, FA) and Mixed anion (I, Br) perovskite
Cu	Copper
CVD	Chemical Vapor Deposition
DC	Direct current
DC	Direct current
DCB	1,2-Dichlorobenzene
DCB	Dichlorobenzene
DMF	N,N-Dimethylformamide
DMSO	Dimethyl sulfoxide
DSSC	Dye Sensitized Solar Cell
DSSC	Dye-Sensitized Solar Cells
E	Energy
e.m.f	Electromotive force
E_{CB}	Energy of conduction band edge
E_G	Band gap energy
EG	Ethylene glycol
EQE	Electron Quantum Efficiency
ETL	Electron transport layer
ETM	Electron transporting material

FA	Formamidinium
FAI	Formamidinium Iodide
FDC	Fast deposition-crystallization
FF	Fill factor
FTO	Fluorine doped tin oxide
HOMO	Highest occupied molecular orbital
HTL	Hole transport layer
HTM	Hole transporting material
IPA	Isopropyl alcohol (2-propanol)
IQE	Internal quantum efficiency
ITO	Indium tin oxide
IV	Current-Voltage
J_{MPP}	Maximum current density
J_{sc}	Short circuit current density
JV	Current density-voltage
LUMO	Lowest unoccupied molecular orbital
MA	Methylammonium ion
MAI	Methylammonium iodide
MACl	Methylammonium chloride
$MAPbI_3$	Methylammonium lead iodide
$MAPbX_3$	Methylammonium lead halide
MAPI	Methylammonium lead mixed iodide-chloride
MeOH	Methanol
min	Minute
mp	Mesoporous
NiO	Nickel(II) oxide
NREL	National Renewable Energy Laboratory
OPV	Organic photovoltaic
Pb	Lead
$PbCl_2$	Lead(II) chloride
PbI_2	Lead(II) iodide
PbX_2	Lead halide
PC61BM (PCBM)	[6,6]-Phenyl-C61-butyric acid methyl ester
PCE	Power conversion efficiency
PEDOT:PSS	Poly(3,4-ethylenedioxythiophene) polystyrene sulfonate
PHJ	Planar heterojunction
PL	Photoluminescence

ppm	Parts per million
PSC	Perovskite solar cell
PV	Photovoltaic
R	Reflectance
rpm	Revolutions per minute
R_s	Series resistance
R_{sh}	Shunt resistance
sec	Second(s)
SEM	Scanning Electron Microscope
spiro-MeOTAD	2,2',7,7'-Tetrakis(N,N-di-p-methoxyphenylamine)-9,9'-spirobiuorene
SSE	Solvent-solvent extraction
STC	Standard Test Condition
T	Transmittance
TCO	Transparent Conducting Oxide
TiO_x	Titanium oxide
UV-vis	UV-visible spectroscopy
v/v	Volume ratio
V_{MPP}	Maximum Power Point Voltage
V_{OC}	Open circuit voltage

Chapter 1

Introduction

Energy access is the "golden thread" that weaves together economic growth, human development and environmental sustainability[1]. Energy has always been a burning issue in Africa, with the provision of access to modern energy in the remotest parts of the Sub Saharan Africa (SSA) being the center focus. This can be attributed to the fact that energy is the backbone of an economy and hence Africa must rise up in solving the energy trilemma of sustainability, affordability, and adaptation to climate change which are the challenges facing the modern world.

With a sprouting population of more than 620 million people, the lack of access to electricity is over 80% in rural areas, where 70% of solid biomass is solely for cooking. It is pertinent that the governments and partners in African countries re-imagine Africa's energy future and no longer depend on traditional approaches to meet the need of our growing economies. To successfully run a continuous and uninterrupted economy Africa requires an efficient energy security approach, as a means of leveling up the economic gap between her and developed countries. To achieve this a sustainable use of her renewable energy resources must be deployed at a greater scale.

Africa's renewable energy resources are diverse, unevenly distributed and enormous in quantity almost unlimited solar potential (10 TW), abundant hydro (350 GW), wind (110 GW) and geothermal energy sources (15 GW)[2]. Compared to other renewable energy resources, the solar resource is more evenly distributed across the continent.

Solar energy is basically energy from the sun's radiation on earth. The light component can be converted directly into electricity with the use of photovoltaic devices while the thermal radiation from the sun, with the use concentrators are used for several heating purposes and indirectly for generation of electricity. Solar Photovoltaic(PV) is a renewable energy technology that utilizes the PV-effect phenomenon existing in semiconductor material in order to convert solar energy directly into electricity in the presence of both direct and diffuse solar irradiation.

One of the benefits of this technology is 'decentralization', hence has been widely exploited for several off-grid/rural electrification projects in SSA. International Energy Agency projects that between 2017 and 2030 within the SSA, on-grid connections would account for 15 GW of new capacity. Within the same period, decentralized solutions, including mini-grids would become a more prominent feature of access, and account for 11 GW of which 30% is solar PV, providing access to electricity in rural areas that complements on-grid connections[2].

The commercially available Solar PV technology is most the polycrystalline and monocrystalline silicon-based solar cells for rural electrification is hindered by several challenges such as the cost of PV panels, efficiency, energy storage, etc. In order to overcome these hurdles especially with regards to the cost polycrystalline solar cells, this research will be focused on organic-inorganic perovskite solar cell a cheaper alternative to silicon solar cell.

1.1 Overview of Photovoltaic technologies

The photovoltaic (PV) effect discovered by Becquerel in 1839 [3] is the basic physical process, by which the semiconductor material converts electromagnetic radiation (sunlight) into electric power. The discovery formed the foundation for research into solar cells and it was only partly deployed for extra-terrestrial applications, in the 1960s photovoltaics received its major support from the space industry for research and development of an alternative to grid power supply for satellite applications. However, today it is a rapidly growing and increasingly important renewable alternative to conventional fossil fuel electricity generation, but compared to other electricity generating technologies like hydropower, it is still regarded as an emerging technology.

In solar cells, the energy of sunlight is converted to electrical energy via a conversion process, where light-induced charges are transported and collected into electrodes [4]. In classical p-n junction cells made of inorganic semiconductors like silicon, absorption of photons higher in energy than the band gap excites some electrons from the valence band to the conduction band, generating electron-hole pairs with small exciton binding energy[5]. For example, even thermal energy is sufficient to dissociate excitons into free carriers in a silicon cell and thus most excitons will instantaneously become free charges. The movement of electrons into n-type and holes into the p-type semiconductor side is achieved by the electric field of a depletion region, as illustrated in Figure 1.1 below. Although this general idea is quite similar among all types of solar cells, their precise operation mechanisms are different
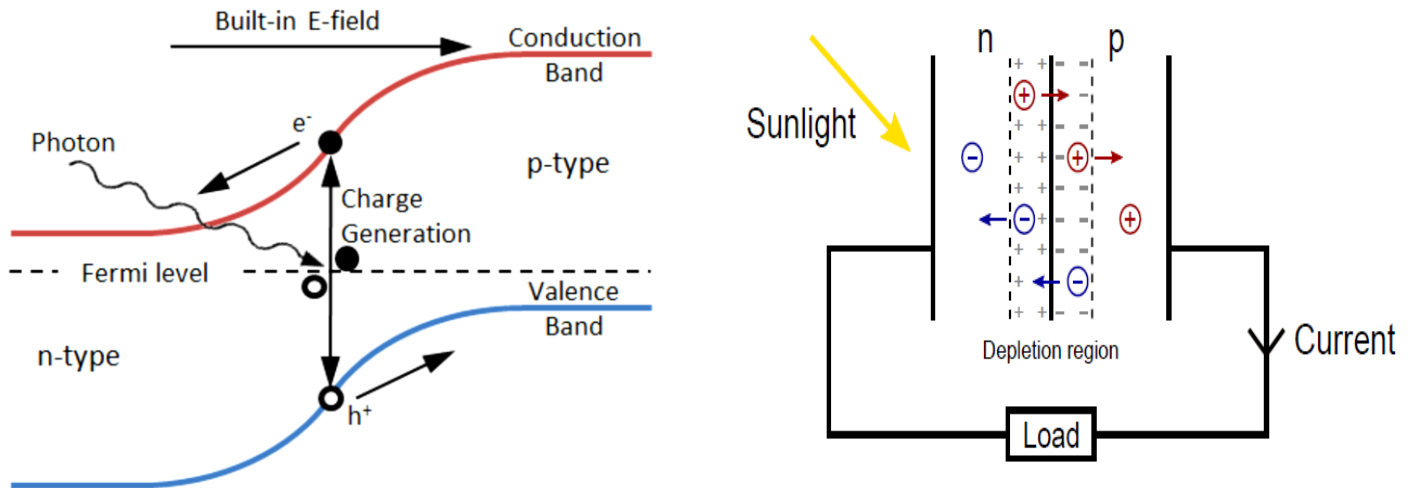
Figure 1.1: A p-n junction band diagram, showing how incident photons cause the charge generation of electron and holes and how the built-in field separates charges.[6] Formed electromotive force (e.m.f) gets the electrons that reach the contact to flow through a connected load to do electrical work [7].

Inserting an intrinsic (i) semiconductor layer between p-side and n-side forms the p-i-n junction, where the electric field is expanded while retaining the built-in bias of the corresponding p-n junction. Such a junction is appropriate for materials, where carriers formed outside the depletion region in p- or n-layers probably cannot contribute to the photocurrent. Carriers formed in the i-layer have often greater lifetimes than in doped materials and are transferred over greater distances towards the contacts. However, in the i-region, smaller conductivities can cause series resistance, recombination is likely at similar electron and hole populations and charged impurities can diminish the electric

field[7]. In p-n and p-i-n heterojunctions, utilization of two dissimilar semiconductor materials with distinct band gaps can enhance carrier collection or be an only option for materials with limited doping properties. Potential step in conduction and valence band edges generates different effective fields for electrons and holes and the alignment of the energy bands critically determines the properties of the junction [5].

Unlike silicon the active 'i' perovskite layer is not doped in order to achieve a built-in voltage, instead the active layer needs heterojunctions with surrounding electron and hole transport layers which have band structures that cause selective extraction of charges when in contact with the band structure of the perovskite active area. The whole heterostructure is built up of a series of materials with band gaps which create an energy landscape to selectively splits electrons and holes towards a cathode and anode [6].

1.1.1 Solar cell Generations

Solar cell technologies have evolved over time from energy-intensive monocrystalline silicon solar cells to roll to roll solution-processed organic solar cells. Hence, solar cells can be classified according to the point in time they started playing a big role in the solar cell field- into first, second and third generation cells [8].

1.1.1.1 First generation cells

They are also called conventional, traditional or wafer-based cells—are made of crystalline silicon, the commercially predominant PV technology, that includes materials such as polysilicon and monocrystalline silicon. About 90% of the commercially produced solar cells are based on this generation.

1.1.1.2 Second generation cells

The cells in this category are designed to address cost issues related to the manufacturing process as they are adapted to cheaper substrates like glass and the thin film could be done via vapor deposition. They include amorphous silicon, CdTe and CIGS cells which are commercially significant in utility-scale photovoltaic power stations, building integrated photovoltaics or in the small stand-alone power system. Regardless of their prospect for providing cheaper devices, this generation of cells would also hit certain price limits per watt due to efficiency limits and the material costs.

1.1.1.3 Third generation Cells

The third generation of solar cells includes a number of thin-film technologies often described as emerging photovoltaics—most of them have not yet been commercially applied and are still in the research or development phase. In addition, the solar cells in this category utilize completely new concepts in terms of device architectures and materials, common examples are Dye-Sensitized Solar Cells (DSSCs)[9], Organic Solar Cells (OSCs), quantum dots solar cells, inorganic-organic perovskite solar cells. DSSCs are based on a combination of dyes with metal oxides and electrolyte. The efficiencies of DSSC are in the range of 12% for small lab scale devices, while the lifetime of the devices is rather low compared to inorganic solar cells. Perovskites began as an alternative sensitizer for dye-sensitized solar cells (DSSCs)[10] but their superior charge transport properties allowed the absorbing layer to thicken. Perovskites have shown an exceptional increase in performance since its inception. Figure 1.2 shows this marked increase in efficiency. The orange line

with yellow circles represents perovskites, in 8 years, the efficiency of perovskite solar

cells has risen to over 20%. The first perovskite cell was described in 2009 and had an

efficiency of 3.8%[10]. Since then, advancements in this field have improved drastically,

with the highest verified efficiency now at 23.3%, measured in 2018[11]. This large increase

in efficiency in such a short time (see Figure 1.2), combined with low

material cost, are two of the biggest reasons why perovskite solar cells have attracted so

much attention.
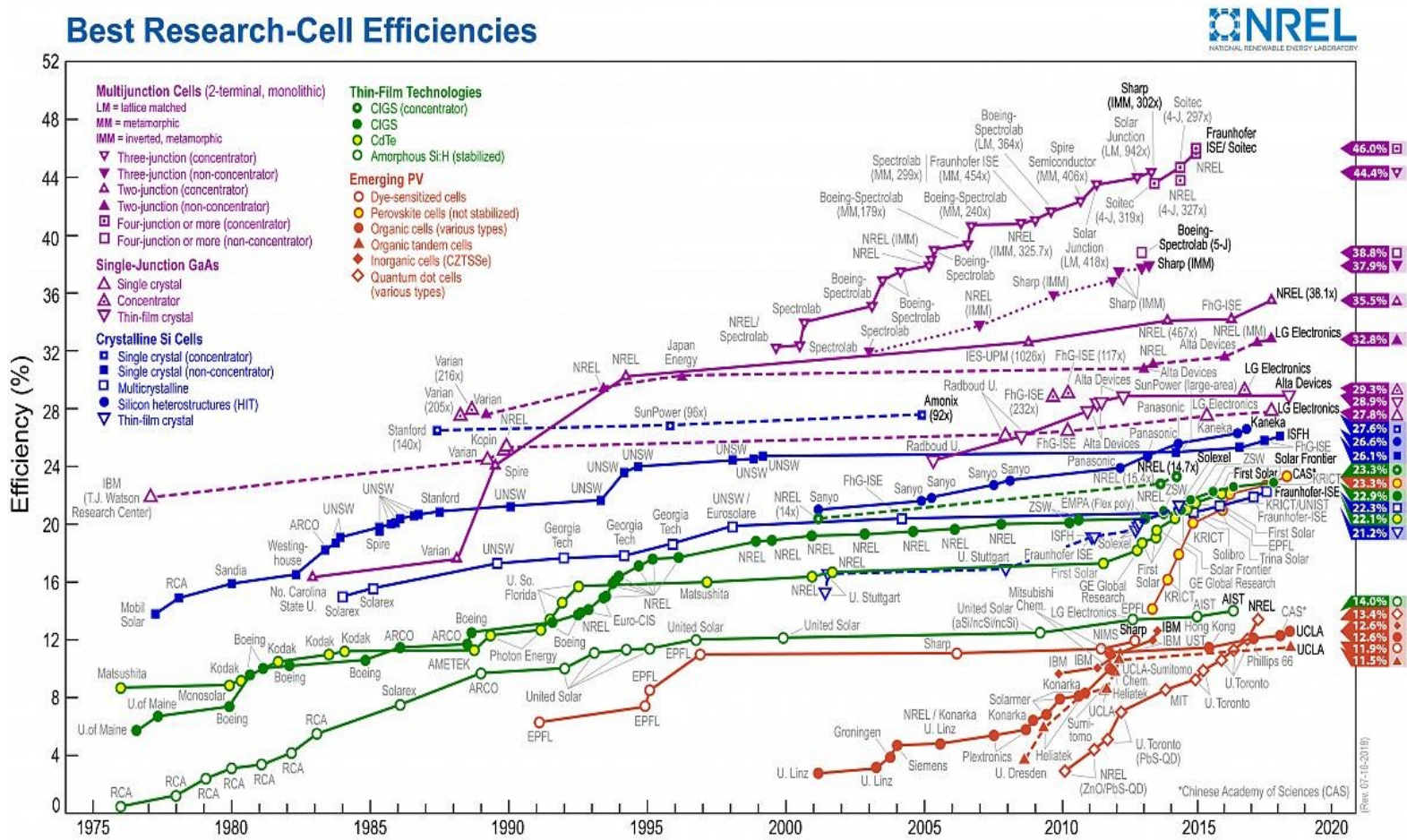
Figure 1.2: Trend of solar cell efficiencies of different PV technologies[11].

1.2 Organometallic Halide Perovskite Solar Cells

The last few years have witnessed the unprecedented rapid development of a new class of solar cells based on organic-inorganic halide perovskites[12]. The perovskite solar cells (PSCs) as commonly called, is a spin-off from research on dye-sensitized solar cells which are liquid electrolyte based solar cells with a photosensitized anode invented by Micheal Graztel alongside with his colleague, Brian O'Regan at UC Berkeley in 1988 [13].

In 2009, Miyasaka et el. was the leading researchers who found that organometal trihalides have light harvesting properties when they are under illumination. used this material in DSSC achieved a high photovoltage close to 1.0V and a maximum PCE of 3.8%[10]. In late 2012, Park et al. fabricated a solid-state mesoscopic perovskite sensitized solar cell and boosted the PCE up to 9.7% [14]. Snaith and co-workers employed a mesoporous alumina scaffold and methylammonium lead iodide chloride to fabricate meso-super structured solar cells (MSSCs), resulting in 10.9% efficiency[15]. Later, the same group further developed planar heterojunction (PHJ) perovskite solar cells, which removed the mesoporous layer and exhibited a PCE of 15.4%[16].

Research on organic-inorganic halide perovskites based solar cells have since been undertaken drastically and skyrocketed to a certified PCE value of 23.3%[11]. This leap can be partly attributed to the fact that perovskite solar cells developed from DSSCs and the materials themselves exhibit properties in common with both organic absorbers and polycrystalline semiconductors, the knowledge gained from these fields thus were invaluable in advancing current understanding[17]. Apart from their extraordinary

photovoltaic properties, organic-inorganic halide perovskites are excellent candidates for the realization of other electronic applications such as lasers, photodetectors, and light-emitting diodes (LEDs) [5, 18].

1.2.1 Crystal Structure of Perovskites

Perovskites, named after Russian Mineralogist L. A. Perovski, initially referred to a calcium titanium oxide mineral composed of calcium titanate ($CaTiO_3$). Such terminology has since been extended to the kind of compounds that take the similar crystal structure as $CaTiO_3$. The class of hybrid organic−inorganic perovskites adopts the general perovskite chemical formula*: ABX₃*

Where *A* is monovalent organic cation typically methylammonium ion $CH_3NH_3^+$ (i.e., MA^+) and formamidinium ion $HC(NH_2)_2^+$ (i.e., FA^+), *B* is metal cation (i.e., Pb^{2+} Sn^{2+}), and *X* is halide anion (i.e., Cl^-, Br^-, I^- or their mixtures).

The formability of this crystal structure can be estimated by Goldschmidt tolerance factor *t*, which is displayed in Equation (1.1) [19].

Where r_A, r_B and r_X are the effective ionic radii for *A* , *B* , and *X* ions, respectively. Another

$$t = \frac{r_A + r_B}{\sqrt{2}(r_B + r_X)} \qquad (1.1)$$

factor, called octahedral factor μ,(see equation (1.2))

$$\mu = \frac{r_B}{r_X} \qquad (1.2)$$

μ is also used to evaluate the stability of perovskite. It is believed that perovskites can be stabilized when t lies in the range of 0.8131 to 0.107 and μ is in the range of 0.442 to 0.895 [19].
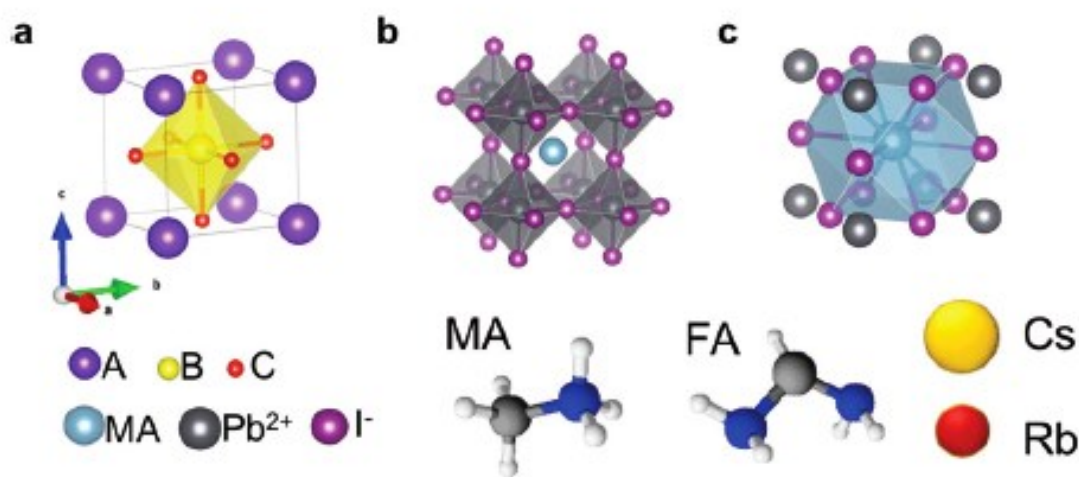
Figure 1.3: Crystal structure features of organometallic halide perovskite[20]

Figure 1.3a shows the Unit cell of a general cubic perovskite. Figure 1.3(b) shows (Methylammonium lead iodide) MAPbI$_3$ illustrating the octahedral coordination around the lead ions. Figure 1.3(c) MAPbI$_3$ illustrating the cuboctahedra coordination around the organic ion. The ideal structure has cubic symmetry and is composed of a backbone of corner-sharing BC$_6$-octahedra with cuboctahedral voids occupied by the A-cations. If the A-ion is small, or the B-ion is large, the tolerance factor (t) decreases below 1 and orthorhombic, rhombohedral, or tetragonal structures are favored rather than the ideal cubic structure[21].

1.2.1.1 *Crystal structure and Phase transitions*

There are several organometallic halide perovskite compounds which can be used for photovoltaic applications. Amongst them, methylammonium lead triiodide $CH_3NH_3PbI_3$ (or $MAPbI_3$), has been most extensively investigated and can, therefore, be seen as a standard perovskite and a model compound. In terms of high-efficiency devices, attention has now shifted away from $MAPbI_3$ towards mixed ion perovskites ($FA_xMA_{1-x}PbBr_yI_{3-y}$)[20].

Given the ionic radii (Pb^{2+} = 0.132nm, I^- = 0.206nm, and $CH_3NH_3^+$ = 0.18nm [22]), the tolerance factor suggests that $MAPbI_3$ should form a tetragonal structure, with PbI_6-octahedra as the backbone with MA^- ions occupying the cuboctahedral voids between them. This is consistent with single crystal data finding $MAPbI_3$ in the tetragonal space group *I4cm* at room temperature[23]. At -113.1°C, a phase transition to an orthorhombic phase[24] and is not suitable for PV applications[25], since this temperature is not experienced in terrestrial environments, it is of no practical concern. As the temperature rises and the thermal energy increases, perovskites commonly go towards a more cubic symmetry[20]. For $MAPbI_3$, a transition from tetragonal to cubic (or pseudocubic) symmetry occurs at around 54.1°C[24]. This is well within the operational window of solar cells and can thus potentially affect the performance of a photovoltaic device. However, the phase transition is slow and reversible and seems not to be problematic for PV applications[25-26].

When the lager FA^+ ion substitutes the MA^+, there is lattice expansion and a change in the tilt of the PbI_6-octahedra which results in a slight decrease of the band gap from ca. 1.59

eV for MAPbI$_3$ to ca. 1.45 - 1.52 eV for FAPbI$_3$ [27]. From the perspective of light absorption, this is a more suitable band gap for a single junction PV device. At room temperature, FAPbI$_3$ is found in a cubic or a tetragonal structure very close to cubic.

One major issue, however, is that the large size of FA results in a higher energy barrier for intercalation between the PbI$_2$ layers during perovskite formation which can be offset by a higher annealing temperature[27b, 28]. This higher temperature phase transition indicates that FAPbI$_3$ is relatively stable compared with common MAPbI$_3$ at higher temperatures. Additionally, the cubic (or pseudocubic) α-phase of FAPbI$_3$ at room temperature easily transforms into a yellow polymorph with hexagonal symmetry which is unsuitable for PV-applications [26b]. Both the chloride and the bromide perovskite are found in a cubic structure at room temperature with transitions to a tetragonal structure at lower temperatures. Therefore, they are used, especially the bromide perovskite to stabilize the α-phase FAPbI$_3$ at room temperature.

In summary, the unique crystal structure of perovskites give them a host of intriguing characteristics such as high absorption coefficient[14], wide absorption range, tunable bandgaps[29], low exciton binding energy[30], long electron and hole diffusion lengths[31], high ambipolar charge mobilities[32], and extended charge carrier lifetime [33].

1.2.2 Device Architecture

Unlike in silicon-based solar where the p-n junction is achieved through doping, for solution-processed thin film solar cells, the p-i-n junction is achieved through layer stack of thin films with different properties for efficient charge generation and extraction. The arrangement or the order of deposition and the interfacial structure of the layers in a solar device is referred to as the device structure or architecture.

In general perovskite solar cell device structures are divided into three categories:

1.2.2.1 *Sensitized structure*

In the sensitized configuration also referred to as the mesostructure (see Figure 1.4), the only difference with dye-sensitized cells, is the replacement of the dye molecules by perovskite. In fact, this configuration was the first generation of the perovskite solar cells in which $CH_3NH_3PbI_3$ perovskite dots formed on the nanocrystalline TiO_2 surface and then Spiro-OMeTAD was infiltrated on top of the perovskite coated mesoporous TiO_2 film[14].
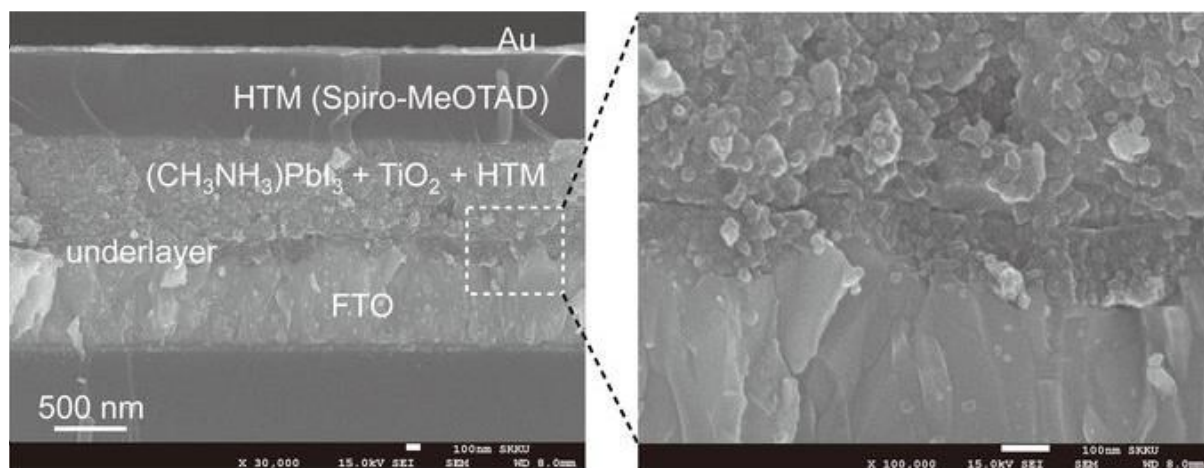
Figure 1.4: Cross-section SEM image of sensitized structure device. (right) Active layer-under layer-FTO interfacial junction structure[14].

1.2.2.2 *Meso-superstructure*

Unlike in the sensitized structure, a continuous thin layer of perovskite rather than dots is deposited such that it infiltrates a mesoporous metal oxide scaffold[15]. TiO_2 and Al_2O_3 are commonly used mesoporous scaffolds and they aid in the electrons and holes transport between cell terminals besides of being used as a sensitizer. Depending on the positions of the charge selective layers; electron transport medium/layer (ETM or ETL) and the hole transport medium/ layer (HTM or HTL) with respect to the glass/ transparent conductive oxide layer (TCO) would determine the configuration of the solar cell.

For the standard or normal configuration (see Figure 1.5a), the ETM is deposited on the TCO/glass substrate before the perovskite active layer, while in the inverted configuration the HTM comes first (see Figure 1.5c).

1.2.2.3 *Planar structure.*

In a planar structure, there is no mesoporous layer and all the layers are compact layers and they form junctions at the boundaries of each layer. In general, there are two configurations of the planar structure, which are called standard (see Figure 1.5b) and inverted (see Figure 1.5d) configurations.
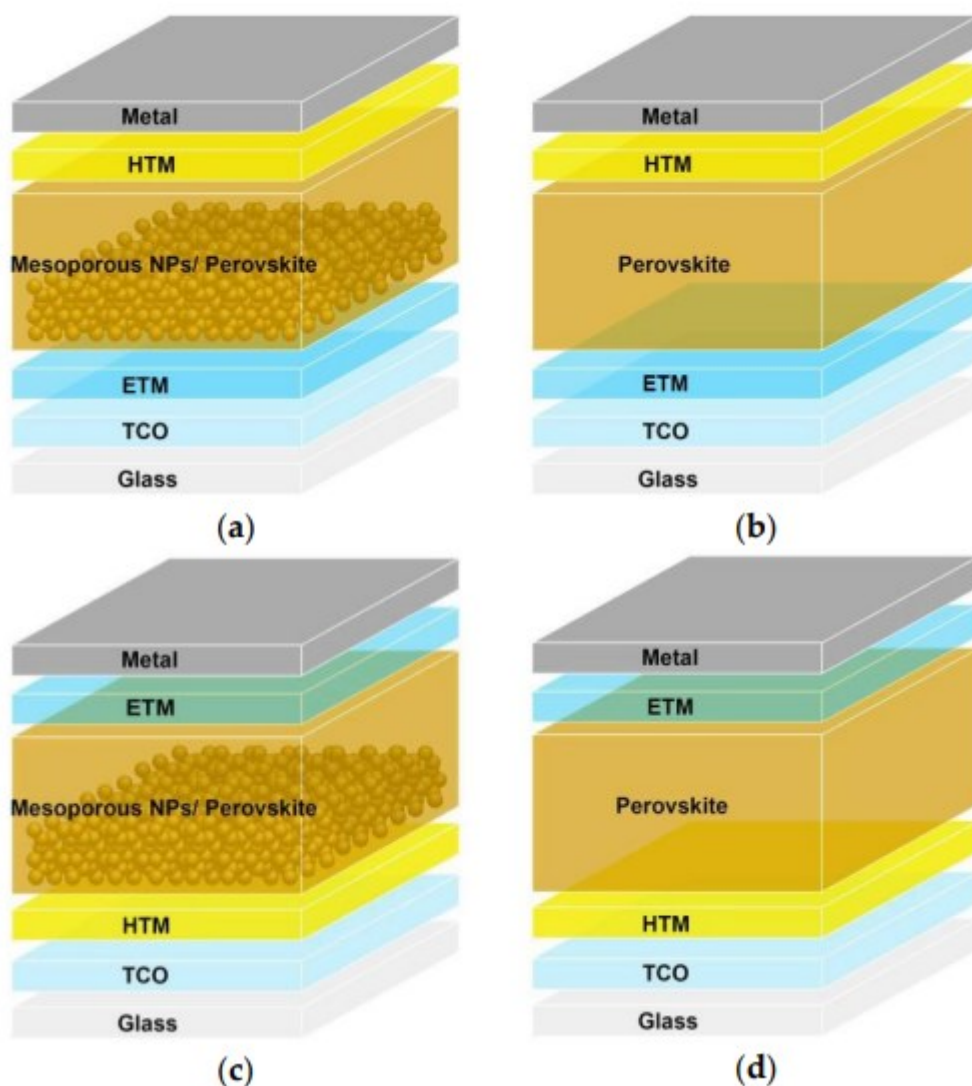
Figure 1.5: Normal and Inverted structures of (a and c) meso-superstructure and (b and d) planar perovskite solar cells respectively.[34]

1.3 The Solar Spectrum

The solar spectrum is distributed over a range of wavelengths from 280 to 4000 nm. The total irradiation at the surface of the earth depends on the length of the path through the atmosphere, which is determined by the orientation of the sun with respect to the normal to the earth's surface at a given location. The length of the path is quantified by a coefficient denoted *air mass* (AM) that has the value 1 for normal incidence. The solar irradiation arriving at the earth fluctuates with the seasons and varies over extended periods of time. However, for energy conversion applications, it is convenient to refer to the operation of devices and processes to a standardized spectrum. Reference spectra are the AM0 corresponding to the spectrum outside the atmosphere and Air Mass 1.5 Global (AM1.5G) that describes the radiation arriving at the earth's surface after passing through 1.5 times a standard air mass, with the sun at 48.2° [5]. Both are shown in Figure 1.6 below. The Standard Test Condition (STC) for solar cells consists of the Air Mass 1.5 spectrum, an incident power density of 1000 W/m^2 (also known as one sun) and a temperature of 25^{0}C.
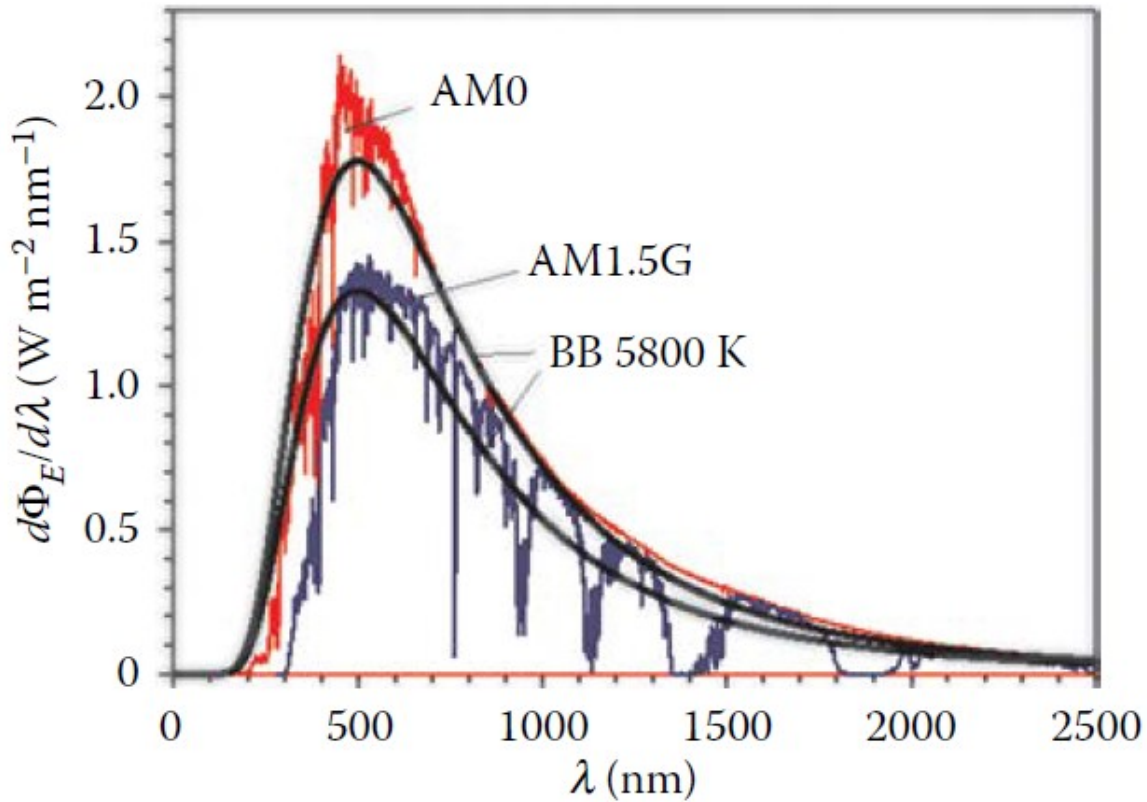
Figure 1.6:The spectral irradiance (energy current density, per wavelength interval) from the sun

just outside the atmosphere (AM0 reference spectrum) and (AM1.5G) terrestrial solar spectrum.[5]

1.4 Solar Cell parameters

Various parameters are utilized for describing the performance of a solar cell. The current-voltage (IV) curve presents the current as a function of voltage and is used to determine the basic parameters and model device's behavior within an electrical circuit[35]. The curves are generated starting the photocurrent sweep from forward bias (V > 0) or reverse bias (V < 0) [36].

The power conversion efficiency (η) of a solar cell is one of its most influential characteristics when discussing its performance. It is based on the parameters open circuit voltage(V_{oc}), short circuit current density (j_{sc}) and fill factor(FF). Another important parameter used to define the efficiency is the maximum power point(MPP), it is the maximum of the current-voltage product. This efficiency of a solar cell can be obtained mathematically as the ratio of the power generated by the device at MPP and the power of the incident radiation $P_{incident}$ as shown in Equation 1.1.

$$s\eta = \frac{J_{sc}V_{oc}\ FF}{P_{incident}} \tag{1.3}$$

Fill factor FF expresses the 'squareness' of the JV curve and is defined as

$$FF = \frac{J_{MPP}V_{MPP}}{J_{sc}V_{oc}} \tag{1.4}$$

In general, the V_{oc} of any solar cell is limited by the energy difference between the quasi-Fermi level splitting of the free charge carriers, i.e., the holes and the electrons, after their transport through the photoactive layer and the interfaces at the contacts. While for ideal (ohmic) contacts no energetic loss at the junction is expected, energy level offsets or band bending at non-ideal contacts will further reduce the V_{oc} [37].
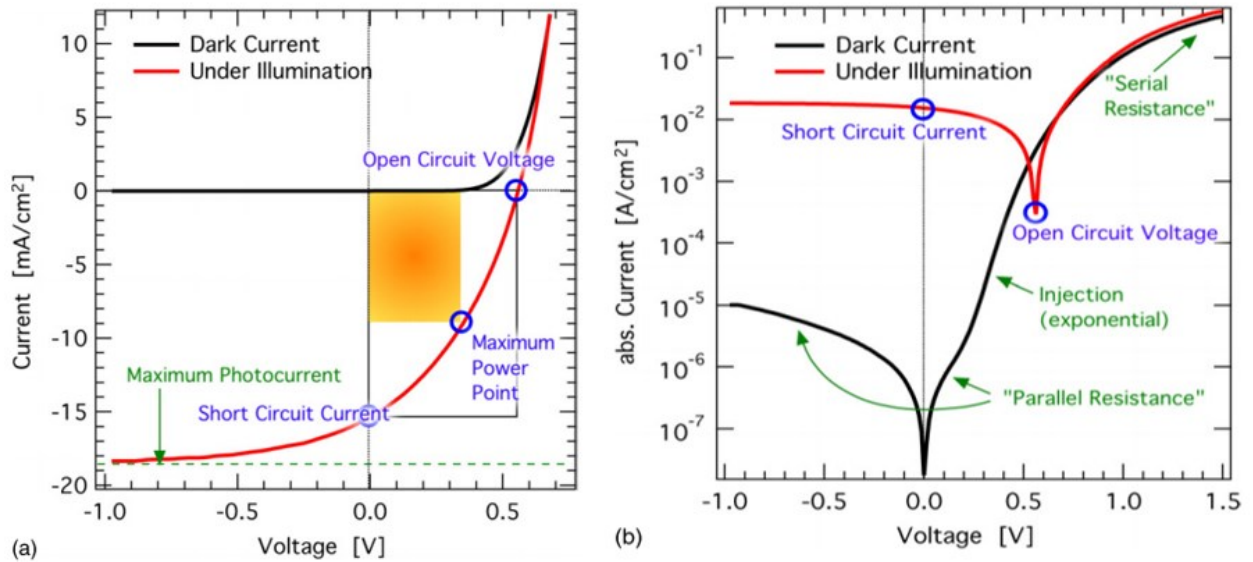
Figure 1.7 Schematic current–voltage characteristics of bulk heterojunction solar cells in (a) linear and (b) semilogarithmic representation[38].

The maximum attainable efficiency is given by the detailed balance limit for inorganic p–n junction solar cells, published by Shockley and Queisser [39]. The famous Shockley diode equation (1.5) though derived for inorganic devices, has been applied by many researchers in the field of organic semiconductors to describe or fit the current-voltage characteristics. The equation is based on an exponential term, as a positive voltage bias leads to the injection of charge carriers into the solar cell. The current increases exponentially, leading to a rectifying behavior in the ideal case.

$$J = J_0 \left[exp\left(\frac{qV}{kT}\right) - 1 \right]$$

(1.5)

Where K is the Boltzmann constant, T is the absolute temperature and J_0 is the reverse saturation current density (typically in p–n junction solar cells, it denotes the current density contributed by minority charge carriers, which is the total of the hole current in the n region and the electron current in the p region) and V is the output voltage [40].
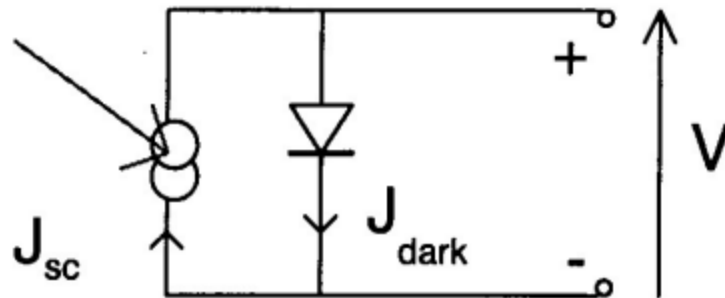
Figure1.8: An equivalent circuit to model an ideal solar cell[41].

For real solar cells, however, the ideal Shockley equation was modified by two resistors. The real solar cells do not achieve ideal cell behavior due to incomplete absorption of incident light, non-radiative recombination of photogenerated carriers and the voltage drop due to the series resistance between the point of photogeneration and external circuit[41]. An equivalent circuit for modeling such a solar cell is presented in Figure 1.9, where two parasitic resistances have been marked in series R_s and in parallel R_{sh} resistance.
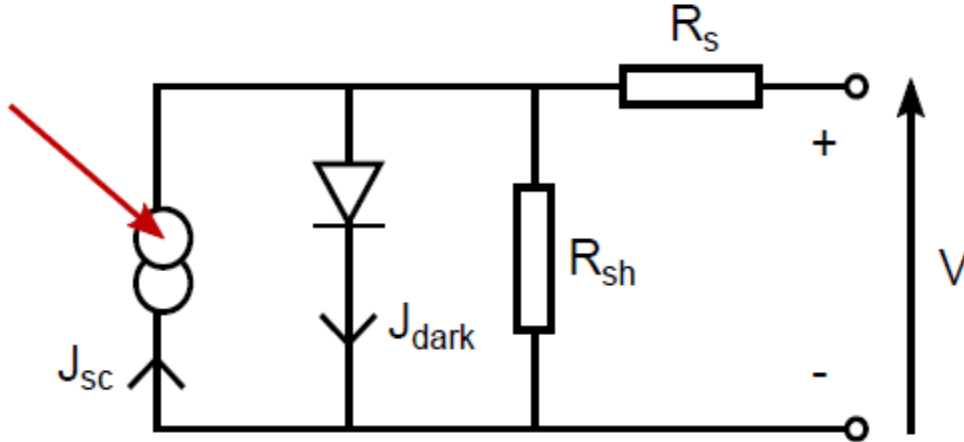
Figure 1.9: An equivalent circuit to model a real solar cell with series and shunt resistances[42].

The series resistance R_s—in series with the ideal diode(see Figure 1.9)—basically describes and accounts for contact resistances such as injection barriers, resistance in the active layer, electrodes and also the interfacial resistance between the contacts of the active layer and the electrodes. While the shunt resistance R_{sh} accounts for leakage currents, which could arise from leakage current in the p–n junction, from the edge of the cell through the cell and between contacts of different polarity. The modified version which describes the real solar cell is a function of R_s and R_{sh} and is given by equation (1.6)

$$J = \frac{R_s}{R_s + R_{sh}} \left\{ J_0 \left[exp \left(\frac{q\ (V - JR_s)}{nkT} \right) - 1 \right] + \frac{V}{R_{sh}} \right\} - J_{ph} \qquad (1.6)$$

Where, J_{ph} is the photocurrent density, n is the diode ideality factor. When, $n =\ 1$, it shows that the recombination of charge carriers in the depletion region is zero (or negligible) and diffusion current is dominant in the device. However, when n =2, then the reverse is the case.

The effect of resistances within a device is seen in IV curves as a reduction of the maximum power point, as can be seen in Figure 1.10. It is desirable to get *Rs* as low and *Rsh* as high as possible[41].
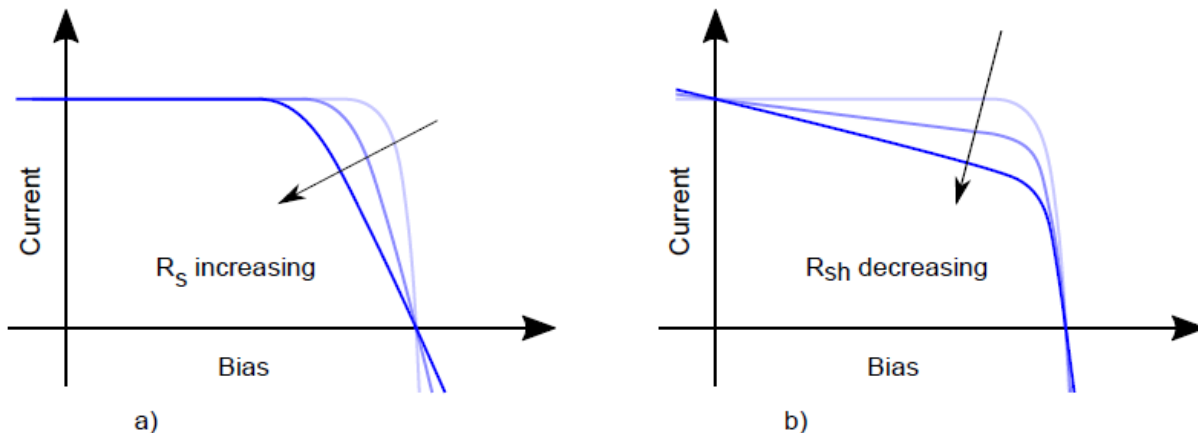
Figure 1.10: The effect of parasitic resistances on solar cell parameters a) Increasing series and b) decreasing parallel [41].

The presented model does not take into account capacitance elements such as charge traps [36], where charge trapping and de-trapping processes cause delayed photocurrent response seen as hysteresis in JV curves[43]. Thus, more complex circuits with capacitors are used to model such cells for identifying charge recombination pathways.

1.4.1 Photocurrent and quantum efficiency

The cell's quantum efficiency QE is the probability that an incident photon of energy E will deliver one electron to the external circuit, and it depends upon the absorption coefficient and the efficiencies of charge separation and collection but not upon the incident illumination. Thus it is used to estimate cell properties under various conditions and it connects to J_{sc}

$$J_{SC} = q \int b_s(E) QE(E) dE \qquad (1.5)$$

where q is the electronic charge and $b_s(E)$ is incident spectral photon flux density, the amount of photons of energy in the range E to $E + dE$ emerging on unit area in unit time. QEs should be high at wavelengths corresponding to high solar flux density. [2]

1.5 Motivation

Much attention has been drawn to clean energy due to the depletion of fossil fuels, increase of energy demand and climate change. Abundant solar energy is one of the promising clean energy resources that have been continuously studied in recent years. The earth intercepts about 1,575–49,837 exajoules (EJ) [44] of solar energy which is under-utilized and would be enough to cater for the world energy demand of approximately 0.4 EJ as reported by IEA [45]. Solar PV technology has the potential of decentralization hence a competent tool for delivering modern energy access to rural communities especially those far away from the grid. According to the WEO 2018 report, the projected installed

generation capacity from solar PV in sub-Saharan Africa (SSA) is estimated to increase from 2% in 2016 to 16% in 2030. This projection is based on adaptation of environmental friendly policies by SSA countries. For this to be achievable alongside with the deployment of solar PV technologies all over the world, the cost of generating energy from solar PVs should be highly competitive compared to the already existing fossil fuel technologies. As shown in Figure 1.1, projected levelized cost of electricity (LCOE) generated using solar PV is 61$/MWh compared to 48$/MWh for conventional combined cycle (natural gas)[46]. Hence there is a need for more research on less expensive solar cells both in material and production wise.
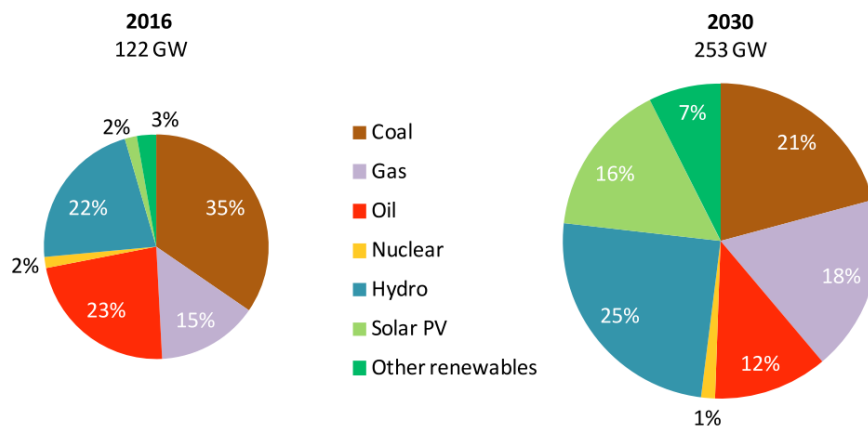
Figure 1.11: Current (2016) versus projected (2030) Installed power generation capacity in sub-Saharan Africa by fuel[1]
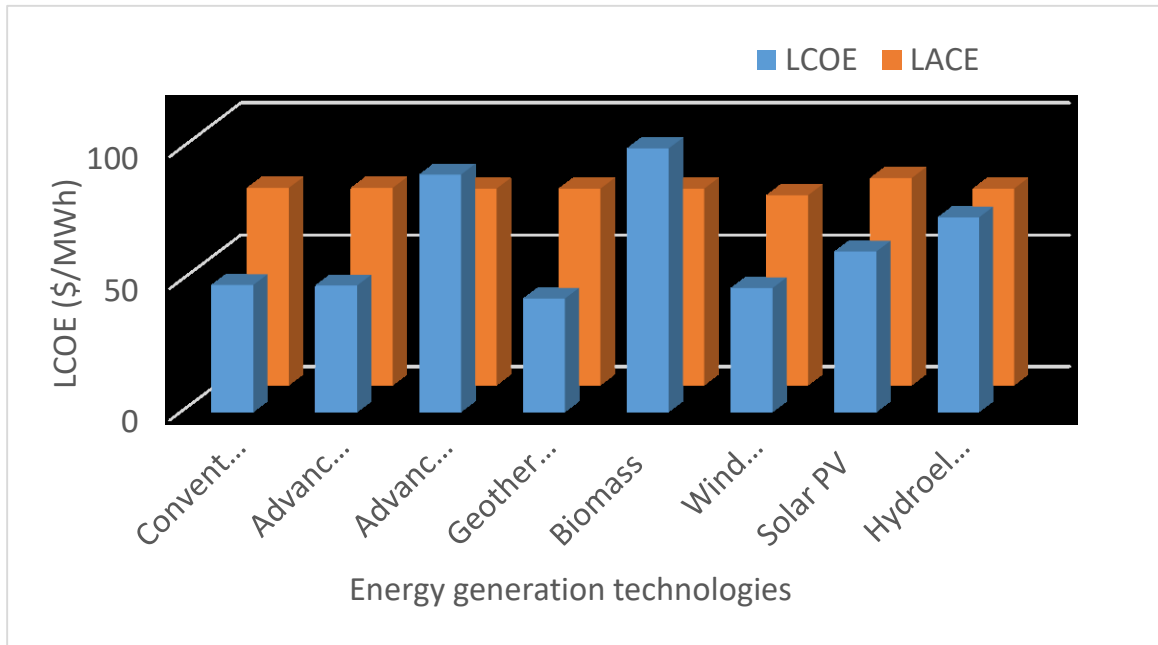
Figure 1.12: The estimated levelized cost of electricity (LCOE) and levelized avoided the cost of electricity (LACE) for new generation resources entering service in 2022 (2017 $/MWh)[46]

Facile to fabricate organic-inorganic halide perovskites solar cells have the potential to become the less expensive alternative to the widely used crystalline silicon solar cells. Silicon-based solar cells are characterized by a high cost, harsh preparation conditions, and serious environmental pollution. Cadmium telluride and copper indium gallium selenium thin-film solar cells have achieved a high efficiency of photovoltaic conversion in the laboratory, but the industrial applications are restricted by the high production cost, environmental pollution, and other problems[47]. As can be seen in Table 1.1 compared to existing PV technologies, perovskite-based solar cells have shown quite a high efficiency and lower energy payback time[48].

Thus the motivation for research Achieving a highly efficient and reproducible organic and inorganic halide perovskite solar cells through facile wet processing. These efficient solar cells will be employing cheaper hole and electron transport layers materials such as PEDOT:PSS and PCBM respectively; and aluminum as the electrode.

Table 1.1:

Comparison of solar cell technologies

Photovoltaic Technology	Power conversion (%)	Diffusion length (μm)	Carrier Mobility (cm²Vs)	Carrier Lifetime	Band Gap (eV)	Loss in Potential (eV)	Stability	Main Elements		Energy Payback time (years)
								Critical	Toxic	
c-Si[17][49]	26.63 ± 0.53	100-300	$10 - 10^3$	4ms	1.1	0.4	> 25 years	-	-	1.7 - 4
GaAs (Thin film)[17]	28.8 ± 0.9	1 - 5	$>10^3$	50ns	1.4	0.3	>20 years	Ga	As	2.3-5
CIGS[17]	21.7 ± 0.6	0.3 – 0.9	$10 - 10^2$	250ns	1.1	0.3	>8 years	In, Ga	-	0.3
CdTe[17]	21.0 ± 0.4	0.4 – 1.6	10	20ns	1.5	0.6	<4.5years	Te	Cd	0.5-1.1
Dye-sensitized[17]	13.0 ± 0.5	0.005 – 0.02	$10^{-2} – 10$	1ns	1.6	0.7	<20 months	Co	-	0.5-1.5
Organic[17]	11.1 ± 0.3	0.005 – 0.01	$10^{-5} – 10^{-4}$	10 - 100μs	1.6	0.7	<25 days	-	-	0.2-4
Quantum Dot[17]	9.2 ± 0.2	0.08 – 0.2	$10^{-5} – 10^{-4}$	30μs	1.3	0.8	<6 days	-	Pb	1.51
Perovskite[17][11]	23.3 ± 0.4	0.1 – 1.9	2 – 66	270ns	1.6	0.5	4-42 days	-	Pb	0.9

1.6 Research Objectives

The objective of this research focuses on the optimization of recipes used to fabricate thin film perovskite planar solar cells. The main goal of optimization of these devices is to increase the PCE of planar reverse structure p-i-n devices, which are made from a series of thin films deposited on patterned Indium Tin Oxide (ITO) substrates, the films in order of deposition are: poly(3,4-ethylenedioxythiophene) (PEDOT:PSS), perovskite, [6,6]-Phenyl-C60-butyric acid methyl ester (PC60BM), titanium oxide (TiOx) and Aluminum (Al) cathodes. Optimization is achieved by investigating the fine details of device fabrication processes, layer by layer optimization, interfacial engineering and by fundamentally varying the chemical route used to produce the perovskite active layer. This research will also focus on improving the reproducibility of the optimized recipes.

Chapter 2

Literature Review

2.1 Charge Transport in PSCs

The organic-inorganic halide perovskite for a few years has been a center of attraction in the field of solar PV materials research. Their unique crystal structure gives them amazing photoelectric features that rivals existing solar cell technologies. As stated in the previous chapter, the materials possess excellent photoelectric properties, as high absorption coefficient[14], wide absorption range, tunable bandgaps[29], low exciton binding energy[30], long electron and hole diffusion lengths[31], high ambipolar charge mobilities[32], and extended charge carrier lifetime [33]. And as such when employed in solar cells, these features lead to a high open-circuit voltage (V_{OC}) and a short-circuit current density (J_{SC})[47].

When the perovskite solar cell is exposed to sunlight, the perovskite layer firstly absorbs photons to produce excitons (electron-hole pairs). Due to the low exciton binding energy prevalent in most perovskite materials, these excitons can easily form free carriers (free electrons and holes) to generate a current or can recombine into excitons. Hybrid perovskites have low carrier recombination probabilities and the higher carrier mobility, thus the diffusion distance and lifetime of the carrier are quite long. For example, the carrier diffusion length is at least 100 nm for $MAPbI_3$ and longer than $1\mu m$ for $MAPbI_{3-x}Cl_x$ [50]. The longer diffusion distance and lifetime of carriers are the source of the superior performance of perovskite solar cells. The photogenerated free electrons and holes are collected by an electron transport material (ETM) and a hole transport material (HTM).

Electrons/holes are collected separately and simultaneously from the ETM/HTM at the back metal electrode/front transparent conductive oxide electrode and subsequently to the outer circuit.
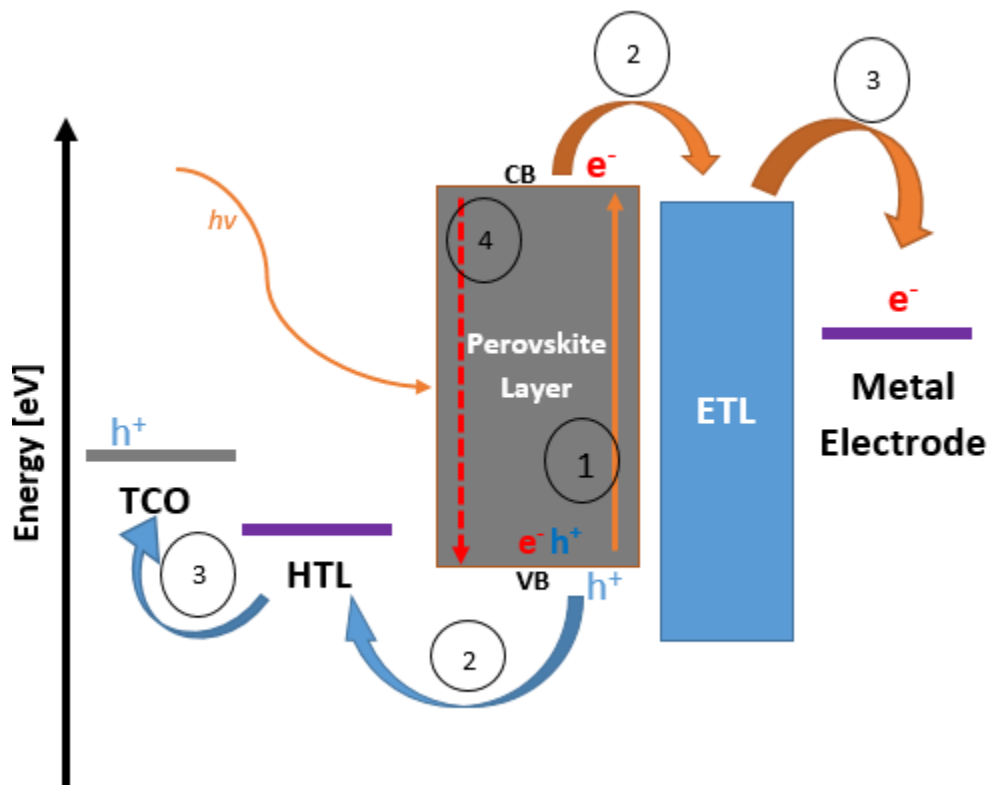
Figure 2.1: Band diagram and main processes and PSC: (1) Absorption of photon and free charges generation;(2) Charge transport; (3) Charge extraction;(4) charge recombination [4].

The representation the of transport processes of electrons and holes in an HTL/perovskite/ETL cell are shown in Figure 2.1. A study by Marchioro et al. shows that the electron-hole pairs separated at the two heterojunction interfaces of HTL/perovskite and ETL/perovskite, followed by electrons injecting into ETL (process (1), see Figure 2.1)

and holes injecting into HTL (process (1)) to achieve charges transport[51]. At the same time, a series of behaviors that are detrimental to the cell's performance, such as exciton annihilation (process (4)), photoluminescence, or non-radiative recombination, as well as reverse transmission of electrons and holes, and recombination at the ETL/HTL interface will also occur.

Achieving a highly efficient PSC implies minimizing as much as possible such behaviors detrimental to the performance of the cell. In this chapter, different approaches taken by several researchers in improving the efficiency of the PSC will be discussed.

2.2 Alloying of Perovskites

Alloying of perovskite to achieve perovskites with mixed cations and/or halides greatly improves the stability of favorable crystal structures and improved photoelectric properties. Using perovskites with mixed cations and halides is quite preferable since the pure perovskite compounds suitable for PV applications come with numerous disadvantages. For example, $MAPbI_3$ has never reached stabilized efficiencies beyond 20%[52]. By introducing Cl into $MAPbI_3$, Stranks et al increased the exciton diffusion length from approximately 100nm to over 1µm in $MAPbI_{3-x}Cl_x$[31].

As stated in earlier (see page 11), using $FAPbI_3$ instead of $MAPbI_3$ is advantageous due to the reduced band gap, which is closer to the single junction optimum and would thus allow for higher solar light harvesting efficiency[39]. However, pure $FAPbI_3$ lacks structural stability at room temperature as it can crystallize either into a photoinactive, non-perovskite

hexagonal δ-phase (''yellow phase''); or α-photoactive perovskite a-phase (''black phase'')[26b, 53] which is sensitive to solvents or humidity [54].

A study by Saliba et al show that introducing some MA stabilizes the perovskite structure and prevents it from transforming into the yellow polymorph, introducing Br allows for tuning of the band gap, which is favorable for tandem applications, and some Br appears to be favorable for the device performance[21]. Also, following this approach they went further to synthesized Cs/MA/FA triple cation perovskites to improve crystal quality achieving reproducible efficiencies above 20%[55].

Therefore, it has become an important design principle to mix cations and halides to achieve perovskite compounds combining the advantages of the constituents while avoiding their drawbacks.

2.3 The inverted Planar Structure

The first inverted planar structure of perovskite solar cells adopted a similar device structure to the organic solar cell [56]. The traditional organic transport layers, poly(3,4-ethylenedioxythiophene):poly(styrene sulfonic acid) (PEDOT:PSS) and a fullerene derivative, were directly implemented as the HTL and ETL in a perovskite device. Through choosing a proper fullerene derivative and optimizing the processing conditions of the perovskite film, a PCE of 3.9% was delivered. Later, Sun et al. succeeded in making a thicker and denser perovskite film by introducing a two-step sequential deposition into the planar device that increased the device performance to 7.41% [57]. After 2013, several attempts were made to improve the efficiency, including film formation and interface

engineering, which will be discussed in the next sections. The main development of the inverted structure perovskite solar cells is summarized in the table below

Table 2.1

Main developments of Inverted structure perovskite cells

Perovskite Processing	HTL	ETL	V_{oc} (v)	J_{sc} (mA/cm^2)	FF (%)	PCE (%)	Ref.
one-step	PEDOT:PSS	PC61BM/BCP	0.60	10.32	63	3.9	[56]
two-step	PEDOT:PSS	PC61BM	0.91	10.8	76	7.4	[57]
one-step (Cl)	PEDOT:PSS	PC61BM	0.87	18.5	72	11.5	[58]
one-step (Cl)	PEDOT:PSS	PC61BM/TiO$_x$	0.94	15.8	66	9.8	[59]
Solvent engineering	PEDOT:PSS	PC61BM/LiF	0.87	20.7	78.3	14.1	[60]
One-step (moisture, Cl)	PEDOT:PSS	PC61BM/PFN	1.05	20.3	80.2	17.1	[61]
One-step (hot-casting, Cl)	PEDOT:PSS	PCBM	0.94	22.4	83	17.4	[62]
One-step (HI additive)	PEDOT:PSS	PC61BM 1.1	1.1	20.9	79	18.2	[63]
Coevaporation	PEDOT:PSS/Poly-TPD	PC61BM	1.05	16.12	67	12.04	[64]
Coevaporation	PEDOT:PSS/PCDTBT	PC61BM/LiF	1.05	21.9	72	16.5	[65]

Two-step spin-coating	PTAA	PCBM/C60/BCP	1.07	22.0	76.8	18.1	[66]
One-step solvent	PEDOT:PSS	C60	0.92	21.07	80	15.44	[67]
One-step (Cl)	PEDOT:PSS	PC61BM/ZnO	0.97	20.5	80.1	15.9	[68]
One-step (Cl)	PEDOT:PSS	PC61BM/ZnO	1.02	22.0	74.2	16.8	[69]
One-step	NiO_x	PC61BM/BCP	0.92	12.43	68	7.8	[70]

2.4 Film Formation Techniques.

Organic-inorganic halide perovskites have the advantage of versatile processability. As can be seen in Figure 2.2, perovskite films can be prepared by chemical and physical deposition techniques, mainly including one-step solution processing, two-step sequential deposition, vapor deposition, and vapor assisted solution processing[16, 71]. It is worth noting that perovskites film quality is susceptible to deposition conditions and also have a huge impact on the solar cell performance[12]. Thus, it is of paramount importance to gain in-depth knowledge of processing approaches, which enables further improvements. In the following discussion, the focus will be on some representative examples to outlined in Figure 2.2.
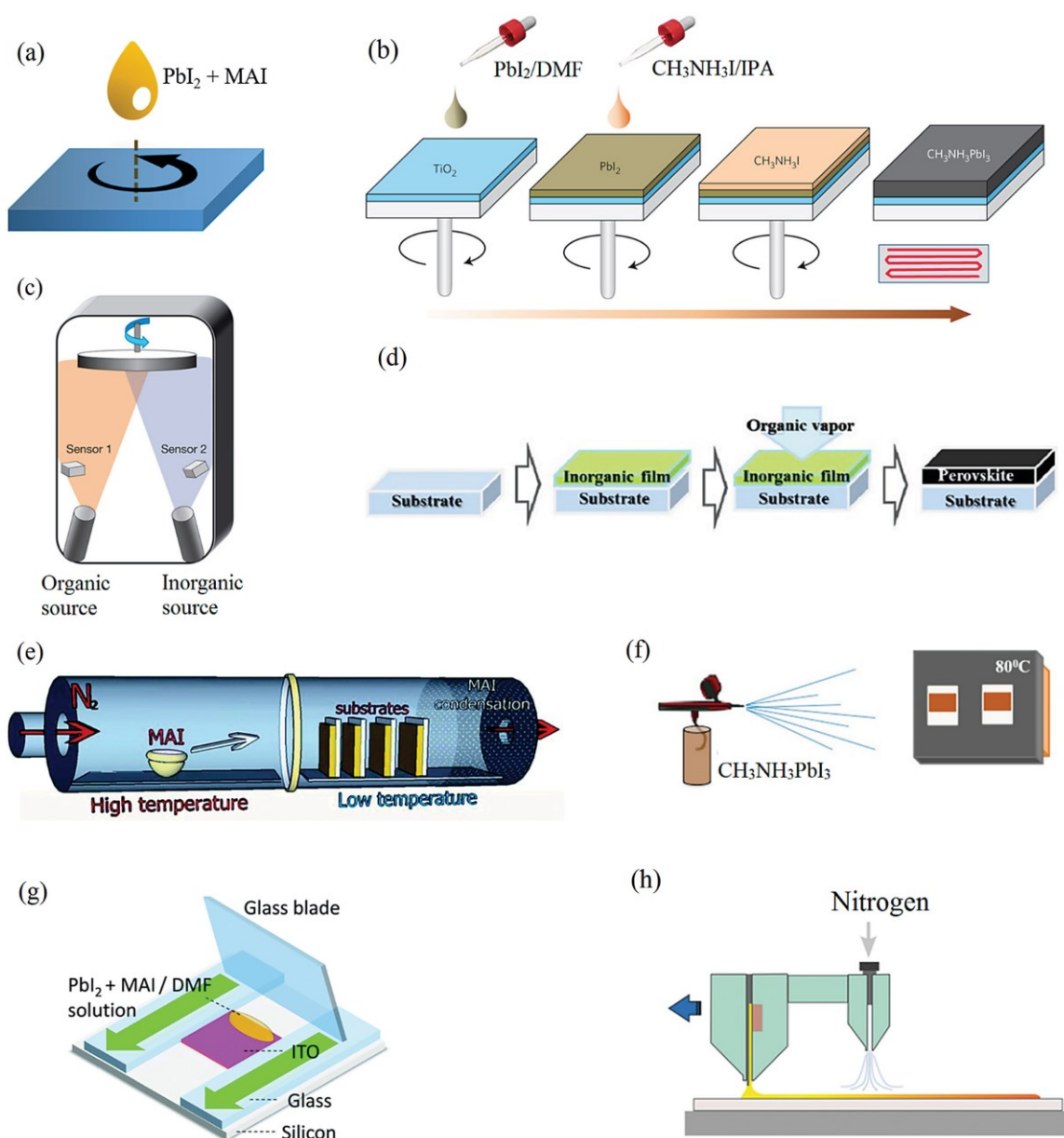
Figure 2.2: Schematic of perovskite film deposition methods.
a) One-step solution processing method. b) Two-step spin-coating procedure[71a]. c) Dual-source thermal evaporation system. Reproduced with permission[16]. d) Vapor-assisted solution process. Reproduced with permission[71b]. e) Hybrid chemical vapor deposition based perovskite synthesis[72]. f) Spray deposition technique. Reproduced with permission[73]. g) Doctor-blading[74]. h) Slot-die coating with a gas-quenching process[75].

One-step solution processing is the simplest one among all the deposition methods. As shown in Figure 2.2a, this method is implemented by spin-coating from a precursor solution of a mixture of PbX_2 and CH_3NH_3X (X = Cl, Br, I) in a polar solvent such as γ-butyrolactone (GBL), N, N–dimethylformamide (DMF) or dimethylsulfoxide (DMSO)[14-15, 76]. The one-step method has the higher potential for scalability since it can be easily applied in large-area full-printing manufacturing.

The one-step method suffers from a major setback of poor coverage and/or pinholes in the spin-coated films, hence the two-step process was developed[77]. The two-step deposition offers a better control of perovskite film morphology[78]. In this method, PbX_2 is firstly spin-coated onto the substrate, followed by dipping or spin-coating of CH_3NH_3X perovskite film (Figure 2.2b)[71a, 77-79]. The two-step deposition method was initiated by Burschka et al.[78], in which PbI_2 was first spin-coated on a mesoporous TiO_2 film and subsequently transformed into $CH_3NH_3PbI_3$ by dipping it into a solution of CH_3NH_3I in 2-propanol (IPA). The Park group later used a two-step spin-coating procedure to produce high-quality perovskite films. It was found that the crystal size of as-made $CH_3NH_3PbI_3$ strongly depended on the concentration of CH_3NH_3I[71a]. Generally, a lower concentration led to a bigger cuboid size.

Such a two-step sequential deposition approach can be modified to obtain mixed halide perovskites. For example, morphology-controllable $CH_3NH_3PbI_{3-x}Cl_x$ perovskites can be prepared by spin-coating a mixed solution of CH_3NH_3Cl and CH_3NH_3I or a mixture of $PbCl_2$ and PbI_2[77, 80]. In another work, $CH_3NH_3PbI_{3-x}Br_x$ was synthesized through spin-

coating CH$_3$NH$_3$Br:CH$_3$NH$_3$I mixed precursor solution onto the PbI$_2$ layers [81]. Interestingly, pseudohalogen thiocyanate (SCN) was introduced into perovskite by spin-coating a mixture of PbI$_2$ and Pb(SCN)$_2$ source in the first step, followed by coating a CH$_3$NH$_3$I layer. The final CH$_3$NH$_3$PbI$_{3-x}$(SCN)$_x$ perovskite films presented larger-sized crystals and fewer traps than CH$_3$NH$_3$PbI$_3$ [82].

2.5 Interface Engineering for Efficient Solar Cell

2.5.1 Hole Transport Layer

The role of the hole transport layer (HTL) is vital to reducing interfacial recombination and effectively extracting charge carriers from the perovskite active layer to the corresponding electrodes. At present, poly(3,4-ethylenedioxythiophene): polystyrene sulfonate (PEDOT:PSS) is one of the most popular hole transport materials used to construct p-i-n-type PSCs[83]. PEDOT:PSS is also widely used in organic solar cells, organics light emitting diodes (OLEDs) and in other optoelectronic devices due to its excellent mechanical flexibility, good thermal stability, and high transparency in the visible range. It can be dispersed in water and several organic solvents and hence PEDOT:PSS films could be prepared by simple solution processes such like spin coating or inject printing or roll to roll printing hence scalable, and applicable in wearable and flexible optoelectronics and solar photovoltaics.[84]

The monomer of PEDOT, EDOT can be chemically polymerized in a poly (styrenesulfonic acid) (PSS) solution to give a PEDOT:PSS water emulsion. The

conjugated polymer PEDOT is positively doped, and the sulfonate anionic groups of PSS are the counterions used to balance the doping charges.[85]
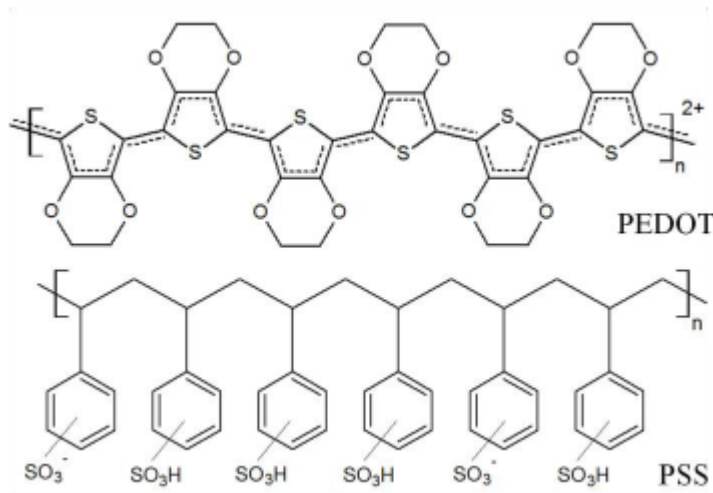
Figure 2.3: The structure of PEDOT:PSS[84].

The presence of the PSS counterion and emulsifier which also have insulating properties can be detrimental to the electrical properties of the PEDOT:PSS as HTL in PSCs. Charge transport within the PEDOT:PSS layer is inefficient because of low conductivity. Inefficient hole transport could create an unbalanced carrier transport, resulting in charge accumulation at the interface that in turn reduces the shunt resistance and increases the leakage current. [83]

The n-i-p regular structure usually shows an open voltage over 1 V, while the inverted structure shows a slight open circuit voltage drop (0.9−1 V) [54, 76b]. Compared to the mesoporous superstructure, the PEDOT:PSS which is a commonly used HTL, yields a perovskite film with inferior crystal quality. The rough mesoporous scaffold tends to serve

as seed crystal for the perovskite crystals which is not the case for the PEDOT:PSS film substrate [86].

In addition, the band alignment between perovskite and the traditional hole transport layer PEDOT:PSS could be another issue. The work function of the generally used hole transport layer PEDOT:PSS is about 4.9−5.1 eV, which is shallower than that of the valence band of perovskite layer (5.4 eV), leading to an imperfect ohmic contact between perovskite and the p-type transport layer and a consequent V_{oc} loss[86]. To address this problem, PEDOT:PSS must be modified or replaced by another material with a high work function. The most common polymers, such as poly-TPD[64], PCDTBT[65] and PTAA [81], with deep HOMO levels ($\sim$−5.4 eV), have been used to modify the PEDOT:PSS surface and the devices based on the bilayer hole transport layer (PEDOT:PSS/polymer) showed an enhanced V_{oc} (>1 V). Unfortunately, these polymers are usually hydrophobic, and thus, the perovskite precursor cannot be coated onto these polymer surfaces.

In order to improve the conductivity of PEDOT:PSS, several methods have been reported, including doping additional organic compounds with their boiling points higher than the boiling point of water, such as dimethyl sulfoxide (DMSO),[83-84] ethylene glycol[85, 87] ionic liquid,[88] salt,[89] dimethyl sulfate,[90] or polyol,[91] into PEDOT:PSS aqueous solution and processing post-treatment of PEDOT:PSS films with cosolvents,[92] ethylene glycol (EG)[93], methanol,[94] or inorganic acid.[95] Generally speaking, doping polar solvents into PEDOT:PSS leads to morphology changes including extended grain size and better interconnection between PEDOT chains, whereas post-treatment usually

results in both morphology changes and removal of unwanted PSS on the film surface. Therefore, methods including post-treatment usually show better results than those simply using additives to improve the conductivity of PEDOT:PSS films.[84]

2.5.2 Electron Transport Layer

The basic function of the electron transport layer is to form an electron-selective contact with the perovskite light-absorbing layer to improve the extraction efficiency of photo-generated electrons and to effectively prevent the hole from migrating to the counter electrode so as to enhance the carrier's separation effect and to reduce the recombination.[47]

The basis for the selection of electron transport materials is as follows. Firstly, the *n*-type semiconductors with the higher carrier mobility are recommended. Secondly, the preparation conditions should be mild and the material can be obtained at low temperatures. Fourthly, the band structure should match the perovskite materials.[47]

In fact, the electron transport layer formed by different systems and structures can achieve high power conversion efficiency, indicating that the selection of commonly used electron transport materials is not the main factor that restricts the power conversion efficiency of solar cells [96].

Docampo et al. found that the ability of PCBM (one of the fullerene derivatives, [6, 6]-phenyl-C61-butyric acid methyl ester) and PFN (poly[9,9-dioctylfluorene-9,9-bis(N,N-dimethylpropyl)fluorine]) to collect electrons was better than that of inorganic TiO2 in inverted solar cells. Perovskite solar cells were prepared with PCBM as the electron

transport layer and PEDOT:PSS as the hole transport layer and such cells achieved a PCE of 9.8% [59].

The advantages of using PCBM as the electron transport/collection layers (ETLs) includes photocurrent-hysteresis-free devices, low-temperature processing and high device efficiency[97]. The PCBM in hydrophobic and thus improves the stability of the perovskite layer against humidity.

In a quest to improve the charge transport properties of the PCBM layer, Chiang et al carried out solvent annealing of PCBM. This approach improved the perovskite interface and as such there was significant improvement in both photocurrent (18.13 mA/cm^2 to 19.98 mA/cm^2) and V_{OC} (from 0.93 V to 1.05 V)[79c]. In the same vein, Yuchan et al, achieved two orders of magnitude reduction in perovskites surface traps by fullerene passivation. This surface passivation was achieved by thermal annealing of the fullerene layer which led to double of power conversion efficiency. [36]

Yang et al, introduced in the fullerene layer with n-doping via anion-induced electron transfer, resulted in dramatically increased conductivity over 100-fold. With cross-linkable silane-functionalized and doped fullerene electron transport layer, the perovskite devices deliver an efficiency of 19.5% with a high fill factor of 80.6%. The cross-linked silane-modified fullerene layer also enhances the water and moisture stability of the non-sealed perovskite devices by retaining nearly 90% of their original efficiencies after 30 days' exposure in an ambient environment.[97]

2.6 Solvent engineering and Antisolvent treatment

Solvent engineering involves the exploitation of various solvents with different properties with the aim of improving the perovskite film morphology. The antisolvents are used for solvent extraction such that a uniform crystal growth is induced in perovskite film thus improving the film morphology [12].

Ahn et al highlighted that the poor morphology is likely to be induced by the difference in crystal growth rate between low solubility PbI_2 and high solubility MAI, while DMF is rapidly evaporating[98]. However, they achieved highly densified $MAPbI_3$ films from a one-step DMF DMSO co-solvent precursor. The rapid evaporation of DMF during spinning was controlled by washing with a non-polar diethyl ether (antisolvent) while spinning. This selectively washes away the DMF leading to the formation of $MAI \cdot PbI2 \cdot$ DMSO adduct which decomposes on annealing to yield a pinhole-free film.

In principle, the antisolvent is usually highly miscible with the perovskite precursor solvent but a poor solvent for perovskites. Exposing a wet and spinning perovskite film to the antisolvent rapidly reduces the solubility of perovskite in the mixed solvent, leading to its fast crystallization as a result of decreased Gibbs energy[76b]. Antisolvent treatment can also remove residue halides and ions [99]. The remnant solvents are removed and crystallization further promoted by subsequent thermal annealing. The process is called a fast deposition-crystallization (FDC) process, which has been reported to result in full coverages with micron-sized grains [100]. Similar solvent extraction- induced crystallization

has also been used in a solvent-solvent extraction process (SSE), where a wet polar single-step solution coated film is immersed in a second non-polar solvent bath [47].

In summary, several approaches used by different in improving the optoelectronic properties of the different layers making up the solar cell and other solution processed electronics. We observed that in literature, no research has been done in investigating the effects of PEDOT:PSS and PCBM layers treatment on the crystallinity and solar cell parameters on the mixed cation and anions (CsMAFA) perovskites in planar inverted structure

In this research, the effect of these findings will be investigated on the glass/ITO/PEDOT:PSS/Perovskite/PCBM/TiOx/Al material structure with the aim of optimizing its efficiency. A layer by layer approach of optimization will be adopted while also comparing the effects as the perovskite synthesis route is varied. In this work we show the effects of PEDOT:PSS and PCBM layers treatment on the crystallinity and solar cell parameters on the mixed cation and anions (CsMAFA) perovskites in planar inverted structure.

Chapter 3

Experimental

In this chapter, the materials and the various steps involved in the fabrication of the hybrid perovskite solar cells and thin films will be discussed. Also, the various characterization techniques used in this research will be discussed.

3.1 Materials

Table 3.1 lists the various materials used for this research. The materials were used as received except stated otherwise. The non-anhydrous solvents were dried overnight with the use of molecular sieves.

Table 3.1

List of Materials used in this research and their suppliers.

Materials	Provider	Product/CAS number	*Batch number*
Active Layer Precursor			
Lead iodide (PbI$_2$)	Chempur	10101-63-0	4780
Lead bromide (PbBr$_2$)	Alfa Aesar	10031-22-8	10720
Lead chloride (PbCl$_2$)	Gefahr	7758-95-4	150301
Cesium iodide(CsI)	Strem Chemicals	7789-17-5	
Formamidium iodide (FAI)	Dyesol	350000	621810
Methyl ammonium bromide (MABr)	Dyesol	301000	663107
Methyl ammonium chloride (MACl)	Merck Schuchardt OHG	593-51-1	S6564620-309
Methly ammonium iodide (MAI)	Dyesol	101000	193305
Hole Transport Layer			
PEDOT:PSS	Heraeus	Clevios P VP Al4083	2015P0137
PEDOT:PSS	Heraeus	Clevios PH 1000	2011P0104
PEDOT:PSS	Heraeus	Clevios PH	9000726245

Electron Transport Layer			
PCBM	Solenne b.v.	[60]PCBM	25-02-15
Buffer Layer			
Titanium oxide precursor	Precursor prepared in-house		06-11-2014
Solvents			
N,N-dimethylformamide (DMF)	J&K Scientific	68-12-2	LM70P15
Dichlorobenzene	Sigma Aldrich	D5,680-2	50796CK-319
Toluene	Sigma Aldrich	89677	BCBC2951
Isopropanol	GPR RECTAPUR	20839.366	16A130506
Chlorobenzene	GPR RECTAPUR	22702.298	10I240513
Methanol	Alfa Aesar	L13255	10166567
Acetone	VWR Chemicals	67-6-1	20063.365
Dimethly Sulfoxide (DMSO)	Acros	67-68-5	1371030
Substrates			
Patterned ITO glass 10ohm/sq	Xinyan Technology Limited	XY10S 25.3mm*25.3mm*1.1mm	XY0315
Not patterned ITO glass 10ohm/sq	Xinyan Technology Limited	XY10S 25.3mm*25.3mm*1.1mm	-
Microscope glass	Thermo Scientific	25.3mm*25.3mm*1.0mm	10742787-2018-07
Electrodes			
Aluminum pellets	Aldrich	L6.3mm*6.3mm 99.999%	MKBQ7753V

3.2 Device Structure

The *planar* inverted structure for perovskite solar cells was adopted in this research. With the layers stack Glass/ITO/PEDOT:PSS/Perovskite/PCBM/TiO$_x$/Al (see

Figure 3.1a). The layer stack for perovskite film characterization is as follows:

glass/PEDOT:PSS/Perovskite (see

Figure 3.1b). All the layers are deposited via spin coating except for the aluminum electrode which is deposited through physical vapor deposition. The direction in which irradiation is flashed on each sample during characterization is shown in Figure 3.1 below.
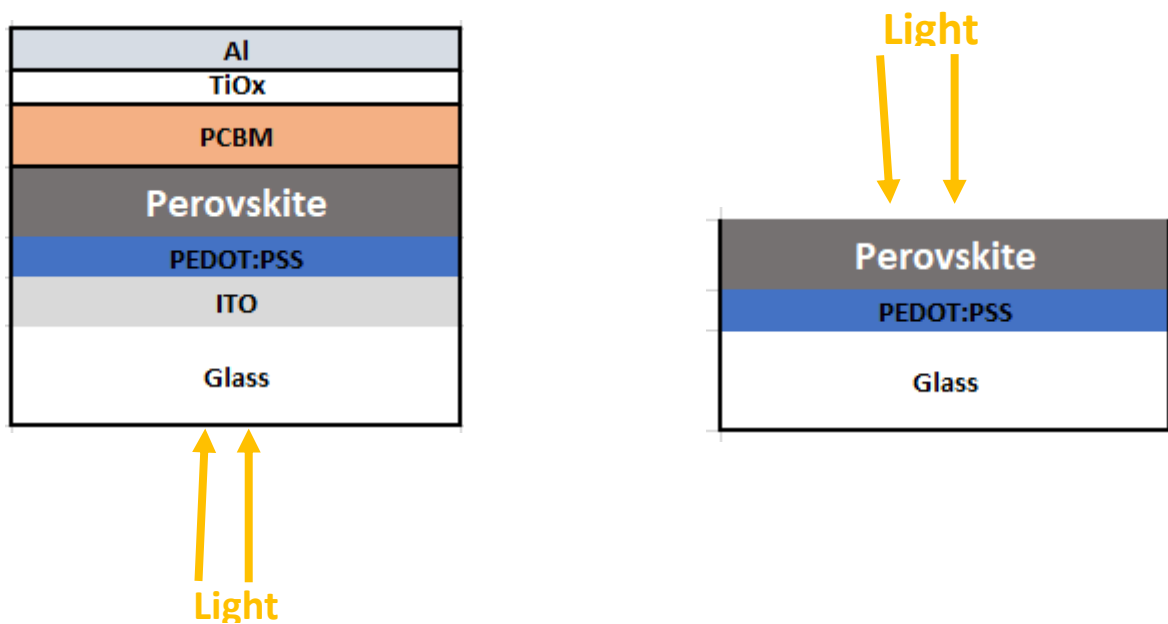
Figure 3.1: L-R the device structure for the solar cell and the layer stack for the thin film.

3.3 Spin coating

The primary fabrication technique for thin film deposition used for data in this thesis is dynamic or static spin-coating. Figure 3.2a demonstrates the spin coating process as it deposits a thin film of solute.

Equation (3.1) is the relationship between spin speed ω and film thickness t.

$$t \, \alpha \, \frac{1}{\sqrt{\omega}} \qquad\qquad (3.1)$$
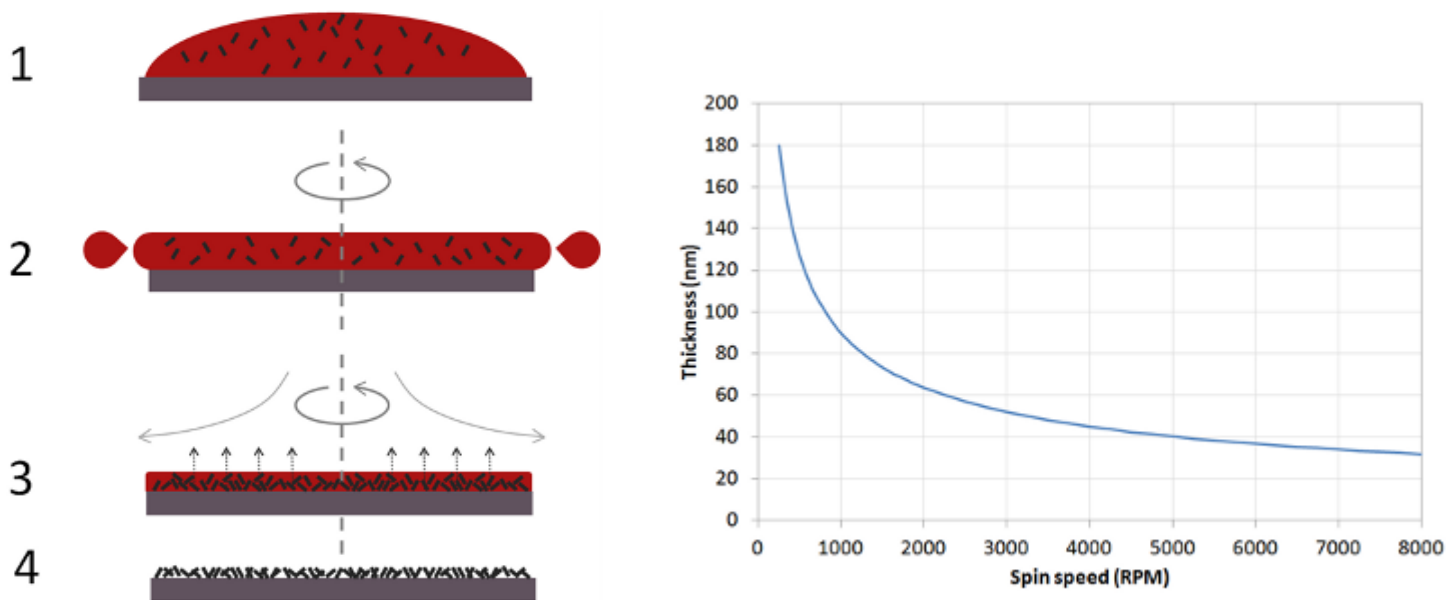
Figure 3.2: (a)Steps 1-4 demonstrate how a solute (black) in a solvent (red) may form a film through spin coating the solution as the solvent evaporates and (b)example of a spin curve for a solution. [101].

For each precursor there is an optimum choice of parameters for spin coating, the parameter space in includes: the viscosity and concentration of the precursor, static or dynamic application of the precursor, spin speed, acceleration and spinning time. Optimizing the spin coating parameters should improve film uniformity, decrease film roughness and remove spin defects and is a simple way to improve the quality of films and hence boost device performance.

3.3 Substrate Cleaning

Before the deposition of the film on the glass/ITO substrate, they are cleaned so to ensure good wettability and uniform film. This is a very important step in solar cell fabrication as it largely impacts its performance. The substrates are first swabbed vigorously with cotton buds soaked in acetone in order to remove glass particles which might be left on the surface after its cutting or after writing the sample name on it. Care is taken so as not to scratch the ITO layer. After which the substrates are sonicated sequentially in a soap solution, deionized water, acetone and isopropanol respectively for 15 minutes for each step at 40°C. Just before the deposition of the hole transport layer, the substrate is dried blowing compressed air over it to ensure uniform drying of the solvent on its surface.

3.4 Hole Transport Layer

In this research, as earlier stated, we used only PEDOT:PSS as the hole transport. This layer is spin coated directly on the ITO /glass or glass substrate as the case may be at the speed of 3000rpm for 30 seconds. Care was taken to ensure a uniform film as the morphology of the PEDOT:PSS layer greatly impacts the outcome of the active layer.

After spin coating, it is annealed at 150°C for 20 minutes. In some of the experiments aimed at improving the hole conductivity, the PEDOT:PSS was doped with methanol while in other experiments, the PEDOT:PSS layer was post-treated after annealing. The post-treatment of the PEDOT:PSS layer was carried out by spin coating different polar solvents

such as methanol, DMF, DMSO etc. on the PEDOT:PSS layer at 3000rpm for 30secs and then annealing again at 190°C for 10 minutes in order to drive off the residual solvent in the film.

Since the PEDOT:PSS layer is highly hygroscopic and is processed outside of the glovebox, it is always transferred quickly into the glovebox whilst hot immediately after the last annealing step. This is to ensure that the PEDOT:PSS film absorbs a minimal amount of moisture from the atmosphere.

3.5 Active Layer.

The perovskite active layer is usually spin-coated on the glass/ITO/PEDOT:PSS or glass/PEDOT:PSS substrate as the case may be. In this research, three different synthesis routes were used to achieve the perovskite active layer. Precursor preparation and deposition processes of these different routes of perovskite will be discussed in the following subsections. The depositions and treatment of the active layer and any other layer after the active layer took place in the nitrogen filled glove box with water and oxygen levels lower than 1 ppm.

3.5.1 One Step mixed halides

This recipe for the one step mixed halide perovskite ($CH_3NH_3PbI_{3-x}Cl_x$) was derived from the work of Wang et al.[102]. The perovskite is essentially a product from reacting lead halide salts (PbI_2 and $PbCl_2$) with methyl ammonium iodide (MAI) as shown below:

$$PbI_2 + MAI \rightarrow MAPbI_3 \tag{1}$$

$$PbCl_3 + 3MAI \rightarrow MAPbI_{3-x}Cl_x + 2MA(g) + (2 - 2x)HCl(g) + HI(g) \tag{2}$$

$$MAPbI_3 + PbCl_2 + 3MAI \rightarrow 2MAPbI_{3-x}Cl_x + 2MA(g) + (2 - 2x)HCl(g) + 2HI(g) \quad (3)$$
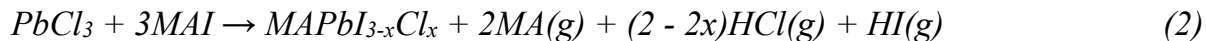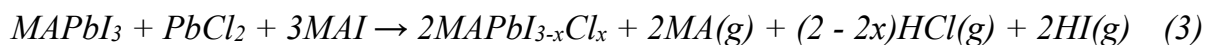
Reaction 3 associated with the formation of the perovskites can be described as reaction 1 followed by reaction 2[102]. Sublimation of some of the products in reaction 3 necessitates having MAI in excess in the precursor.

The precursor of the one step mixed halide is prepared by dissolving 1:1:4 moles of PbI_2 (461 mg), $PbCl_2$ (278 mg) and MAI (700 mg which is in excess of 64 mg) respectively in DMF (2.25 mL). The solution is stirred overnight at 70 °C to ensure complete dissolution.

The completely clear precursor is filtered with a 0.45 μm PTFE syringe filter. It is spin coated on the substrate by in a two-step spinning program (1500 rpm for 18 secs and then 2000 rpm for 5 sec) to ensure better coverage and good film morphology. The film is annealed at 100 °C for one hour immediately.

3.5.2 Two Step Mixed halides

This recipe was adapted from a research of Tripathi et al [103]. The perovskite achieve through this route is $CH_3NH_3PbI_{3-x}Cl_x$ which is similar to the previously discussed route, but unlike the previous, the chloride ion source is MACl and the organic and inorganic salts were dissolved separately.

The precursor is preparing solutions of PbI_2 in DMF 400 mg/mL, MAI in anhydrous IPA 40 mg/mL and MACl in anhydrous in IPA 40 mg/mL respectively in separate vials. Then 4:1 volume ratio of MAI:MACl solutions are mixed in a separate vial. MACl has a

very poor solubility in IPA, as such the solution allowed to settle and only the clear part is used in the preparation precursor. Prior to spin coating, all the solutions are filtered using 0.45 microns PTFE syringe filter.

The PbI_2 solution is first spin-coated on the substrate by dropping 100 μL using a micropipette, then spinning at 3000 rpm for 45 sec followed by drying of the film at 100 ºC. The film is allowed to cool to room temperature after which the MAI:MACl is spin coated at 3000 rpm for 45 sec followed by annealing at 100 ºC for one hour.

3.5.3 One Step Mixed cations and mixed halide

Mixed cation and halide perovskite $Cs_5(FA_{0.83}MA_{0.17})_{95}Pb(I_{0.83}Br_{0.17})_3$ (shortened to CsMAFA) recipe was adapted from the protocol prepared by Saliba et al [55]. The CsMAFA precursor is quite sensitive to storage temperature and cannot be stored for long as such needs to be used right after preparation. The first step involves the preparation of 1.5M stock solutions of the inorganic salts: PbI_2 691.515mg/ml (1.5M) in DMF/DMSO 4:1 v/v and PbBr (1.5M) 550.515mg/ml in DMF/DMSO 4:1 v/v heated at 180 ºC in the glove box until complete dissolution. CsI 389.715mg/ml in DMSO (1.5M) heated at 150 ºC until complete dissolution. All in different vials.

Then followed by the preparation of the $FAPbI_3$ and $MAPbBr_3$ precursors at room temperature:

FAPbI$_3$: FAI (0.1g) + PbI$_2$(0.468ml of 1.5M stock solution) + 0.001mL DMF/DMSO 4:1 v/v.

MAPbBr$_3$: MABr (0.1g) + PbBr$_2$(0.704ml of 1.5M stock solution) + 0.016ml DMF/DMSO 4:1 v/v.

The FAPbI$_3$ and MAPBr$_3$ precursors are mixed in ratio 5:1 v/v to form the MAFA mixed perovskite precursor. 4%vol CsI is added to the MAFA precursor to give the CsMAFA precursor. The cesium cation improves the stability of mixed perovskite.

The 100µL of CsMAFA is pipetted on the substrate then spin-coated for 35 seconds at 5000 rpm. While spinning, the film was washed after 10 seconds with 300µL of chlorobenzene as the antisolvent. The perovskite film was annealed right away at 100 ºC for an hour. Since the CsMAFA perovskite is sensitive to solvent vapor during its film formation, the spin coating chamber is dried with a hairdryer in between each sample. This aims at getting rid of residual solvent vapor in the immediate environment of film formation and ensure the reproducibility.

3.6 Solvent vapor and Methylamine Gas Annealing.

The solvent vapor annealing was carried out on the perovskite films right after spin coating using the method described by Xiao et al [79b] whilst in the glovebox. The films were placed on the hot plate at a temperature of 100 ºC then covered with a petri dish. After which, 10 µL of DMF was added towards the edge of the petri dish so as not directly come into contact with the films (see Figure 3.3). The covered petri dish traps the DMF vapor

thus creating a DMF atmosphere which interacts with the perovskite film. This annealing process was carried out for one hour.
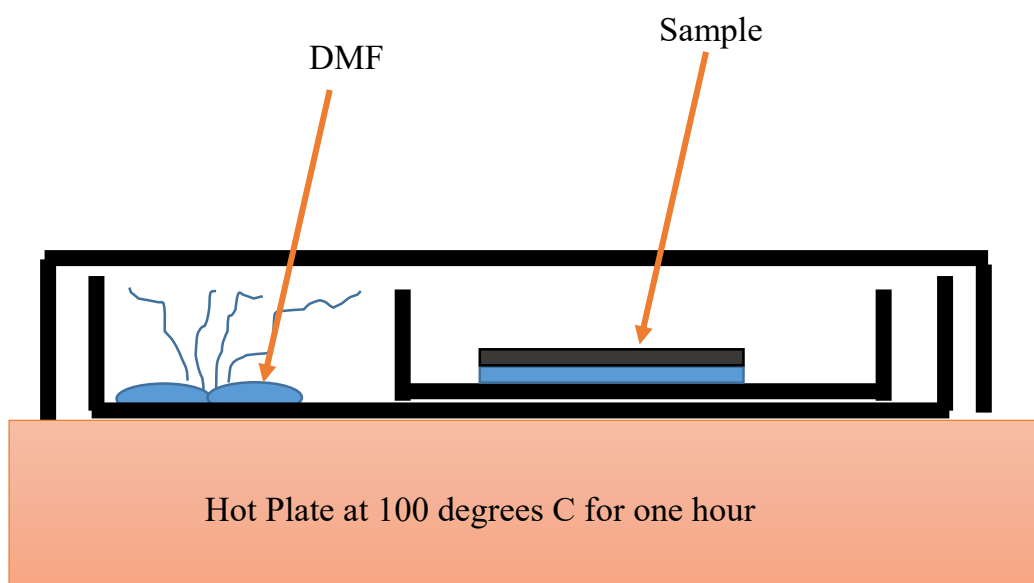
Figure 3.3: The schematic of the solvent annealing setup.

The methylamine gas 'annealing' of perovskite thin film was first reported by Zhou et al in 2015[104]. It is achieved by interacting the perovskite film with methylamine gas to achieve improved crystallinity and better film morphology. Since methylamine gas was not readily available in our lab, the reaction of a methylammonium chloride solution with a strong base was used to produce the gas. The perovskite film was treated with methylamine gas right after thermal annealing.

First, saturated solutions of KOH and CH_3NH_3Cl in dry methanol at room temperature were prepared in separate vials. As shown in Figure 3.4, the substrate is placed in a small petri dish which is in a larger petri dish. Equal amounts saturated solutions of

KOH and CH_3NH_3Cl in dry methanol were added dropped into the larger petri dish such that they don't mix. The larger petri dish is then covered and is tilted gently to allow the mixing of the solutions and subsequent release of the methylamine gas just as shown in the chemical equations below:

In the petri dish: $CH_3NH_3Cl(aq) + KOH(aq) \rightarrow CH_3NH_2\uparrow(g) + KCl(aq) + H_2O(l)$
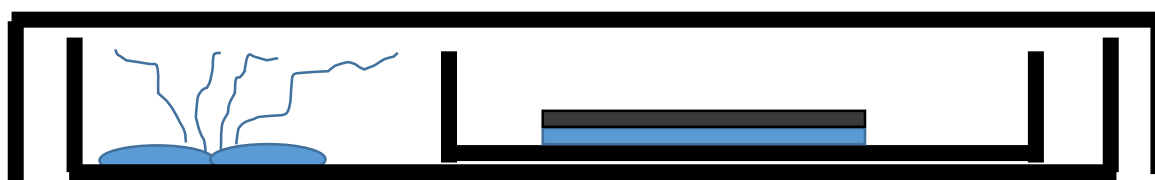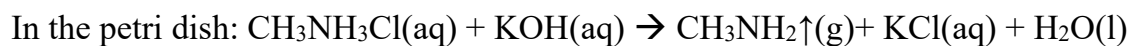
Figure 3.4: Schematic of the methylamine gas annealing set up.

The methylamine gas uptake by the perovskite film leads to 'liquefaction' of the perovskite film Liquefaction occurs after ~5-9 min in the methylamine gas environment. The timer started for annealing after the start of liquefaction the perovskite film which reforms immediately after removal from the petri dish.

3.7 Electron transport layer

The electron transport layer is usually spin-coated on the active layer. The solution was prepared by dissolving 20mg of PC60BM in 1mL of dichlorobenzene. The solution was stirred overnight at room temperature to ensure full dissolution. In the case when a thicker PCBM layer is required the concentration is increased to 40mg/mL. The thickness of the PCBM layer was varied by varying the spin frequency ranging from 600 rpm to 3000 rpm.

Thicker layers were obtained at lower frequencies. After spin coating, the PCBM layer was annealed at 100°C for 45 minutes[36].

3.8 The Buffer Layer and Electrode deposition

Titanium oxide (TiO_x) layer of about 10 nm is sandwiched between the PCBM layer and the aluminum electrode. It prevents the PCBM (and perovskite in case there is a pinhole in the perovskite layer) from reacting with the aluminum electrode. It also functions to improve ohmic contact between the PCBM layer and the electrode while improving the device stability against moisture.[86] Oxygen and airborne water molecules will be adsorbed on the surface of PCBM and resulting in rapid degradation of the PCBM/metal contact. Introducing a thin protective layer, an n-type metal oxide such as TiO_X on top of PCBM can greatly improve the device reproducibility and stability.[68, 105]

According to Lu et al., TiO_x blocking layer should be smooth, dense, and pinhole-free [106]. However, when the TiO_X layer is too thin, pinholes usually form and when thick, a large series resistance is introduced. Both of cases will decrease the device performance. The thin TiO_x layer is formed through the sol-gel process. The TiO_x solution is prepared by diluting concentrated TiO_x precursor 1.5% volume with isopropanol. The TiO_x is dynamically spin cast on the PCBM layer at 3000 rpm for 30 seconds and then annealed for 10 minutes at 100 °C. The substrate is allowed to cool to room temperature.

After which the aluminum electrode is deposited unto the TiO_x layer through physical vapor deposition. A total of 200nm to 300 nm thick aluminum layer is evaporated

at 0.2 0.8 Å/s out of a tungsten boat in a high vacuum using a shadow mask to define the electrodes. Once completed the solar cell is ready for characterization.

3.9 Electro-Optical Characterization

3.9.1 UV-Vis Spectroscopy

This technique is applied for measuring the spectral absorption distribution of the spin-coated films in the wavelength range from near ultraviolet (190-400nm) to visible light (400-90nm). UV-Vis can be applied to distinguish changes in the electronic transitions of the molecules. For this work, the absorption data was obtained simply by shining monochromatic light on the sample film and recording the transmitted light and reflected light. After which the absorption is calculated from the equation below.

$$A = 100 - (R + T)$$

Where, A is the absorbance in %, R is the reflection and T is the Transmission of the deposited film.
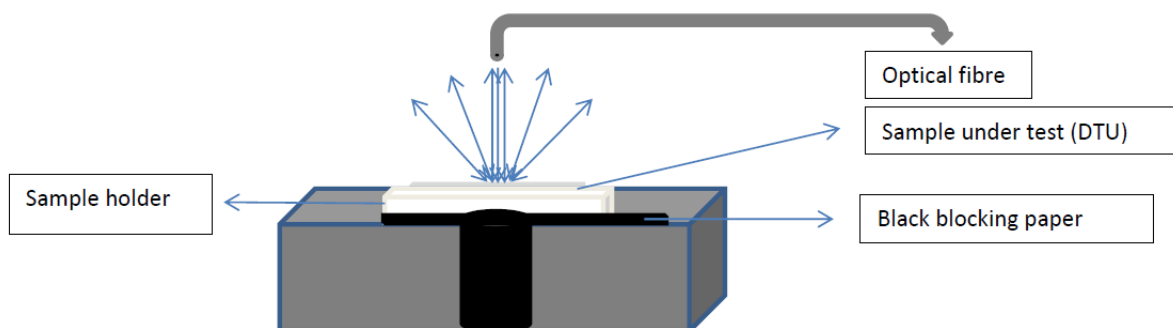
Figure 3.5: Measurement setup for UV-Vis Spectroscopy

The PEDOT:PSS/Perovskite film was deposited on a pure glass substrate. From the absorbance measurements, the optical bandgap of the absorbing semiconductor can be estimated.

3.9.2 Photoluminescence

This is a contactless, nondestructive method of probing the structure of materials. A laser of known wavelength is directed onto a sample, where it is absorbed and excite charge carriers into the conduction band of the sample. The luminescence due to the radiative recombination of the charge carrier is referred to the photoluminescence of the material.

The luminescence intensity provides direct information about the electrochemical potential within the cell; information that is difficult to access through other techniques[107]. The PL technique can be used for comparing the crystallinity of perovskite materials and also to investigate the presence of lead iodide in the perovskite film which can hint to degradation or stoichiometric imbalance(excess lead iodide). In this thesis, steady-state PL spectra were recorded using an Avantes avaspec 2048 fiber spectrometer over a wavelength between 500 and 1100nm at using a laser at 405nm.

3.9.3 IV Measurements

IV measurements were carried out using a two-wire source-sense configuration with a Keithley 2400 in conjunction with Labview software. A LED solar simulator was used for illumination providing approximately 100 mW/cm of AM1.5G irradiation, and the intensity was monitored simultaneously through current and voltage values of LED's power source. To achieve one sun illumination using the LED simulator, the voltage and

current of its power source to adjusted to the calibrated values of 35.2V and 0.6A respectively. The IV measurements were carried out in the nitrogen filled glove box.

After measurements, the obtained data were analyzed using the Origin software.
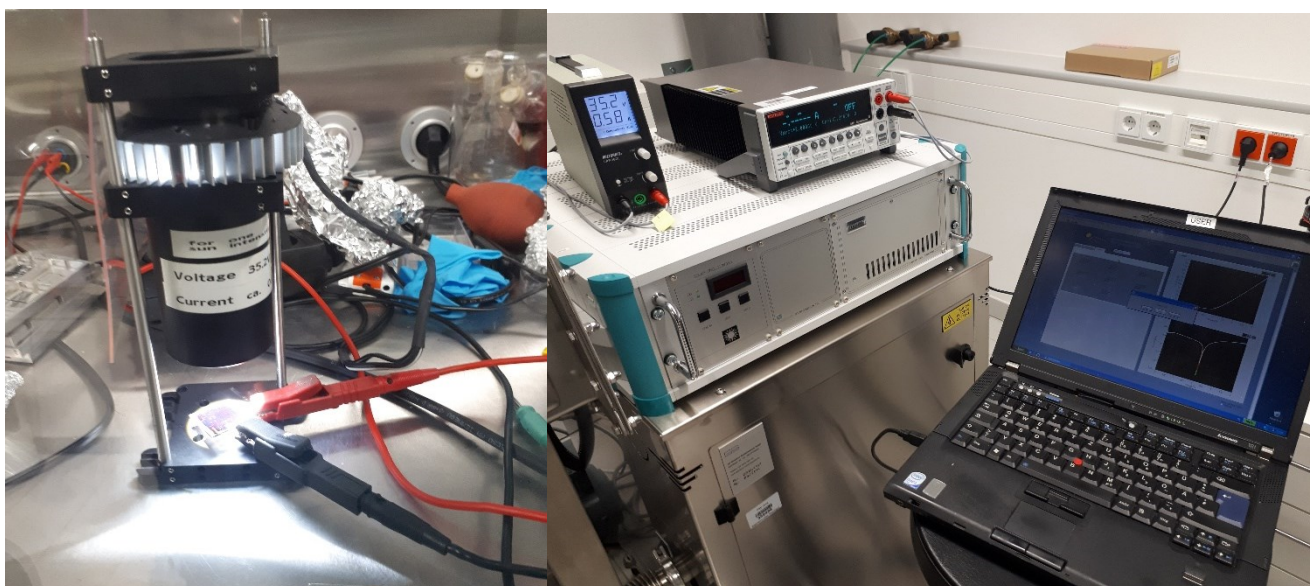
Figure 3.6: The set-up for IV measurements.

3.10 Scanning Electron Microscopy (SEM)

The SEM imaging was carried out on the glass/PEDOT:PSS/perovskite films using the Carl Zeiss Sigma VP scanning electron microscope.

Chapter 4

Results and Discussion

In this chapter results from the various characterization, processes are presented and discussed. Effect of PEDOT:PSS Treatment on Perovskite thin films

4.1 Effect of PEDOT:PSS Treatment on Perovskite thin films

Several ways of treating the PEDOT:PSS has been reported in the literature (see literature review section) with the major aim of improving its charge carrier conductivity. Chou et al have shown in their work that treating the PEDOT:PSS not only affects its conductivity but also impacts its morphology; core-shell structure before treatment to entangled wires structure after treatment [84]. The morphology and crystallinity of polycrystalline perovskite thin films are greatly influenced by the topography of its substrate [96]. Thus in this experiment, we show the impacts of post-treating (AL4083, PH, and PH1000) PEDOT:PSS with solvents (DMF, DMSO, EG, and methanol) on the crystallinity of the CsMAFA perovskite thin film. The absorbance and the photoluminescence spectra of the films are shown below.
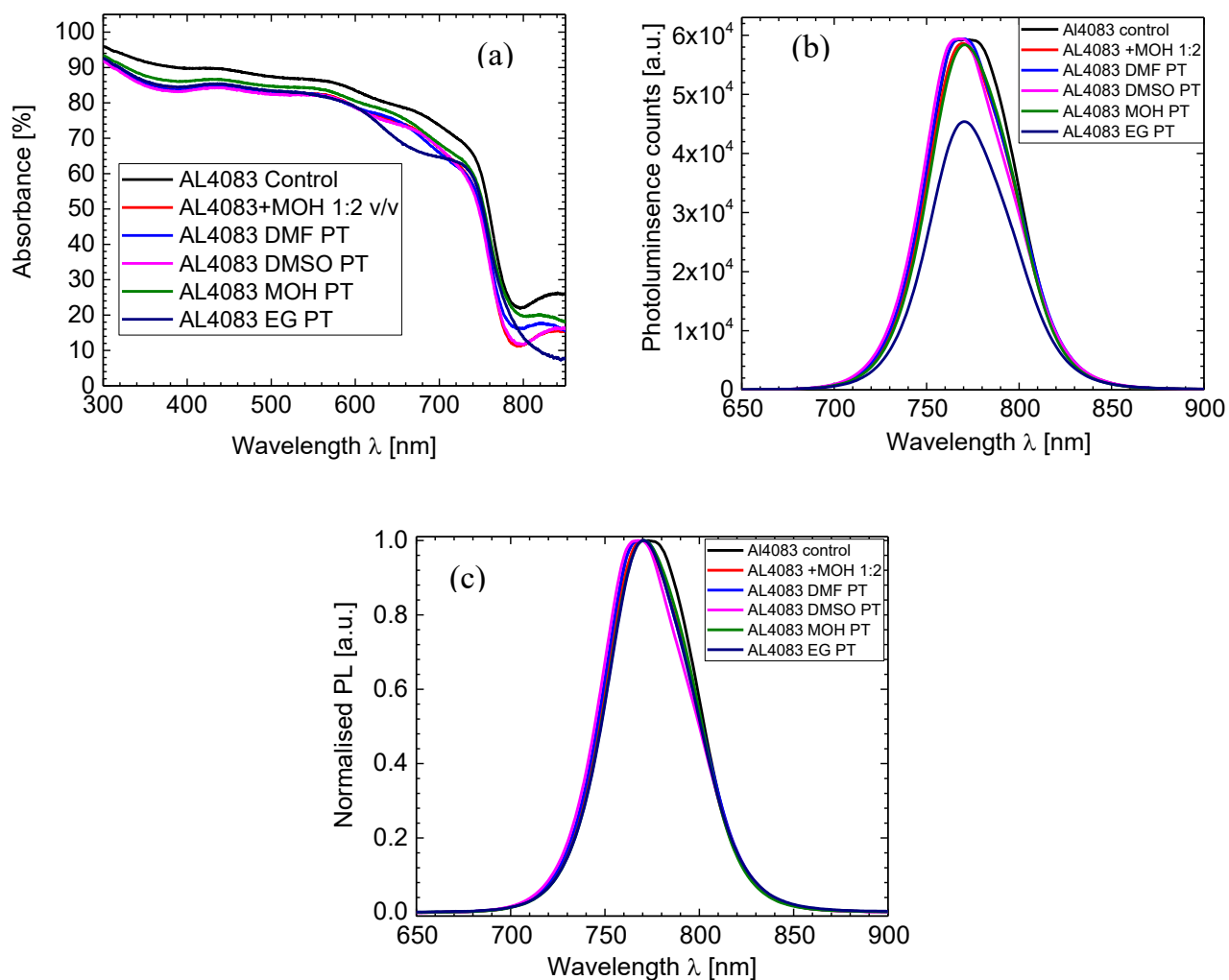
Figure 4.1: (a) Absorbance,(b) PL and (c) Normalised PL spectra of CsMAFA on AL4083

Figure 4.1 shows the absorbance spectra and PL spectra of the CsMAFA perovskite on the treated AL4083 PEDOT:PSS layer. The sample 'control' was neither post-treated nor doped, the sample AL4083+MOH 1:2 v/v was doped with methanol at the ratio of 1:2 and was also not post-treated. Other samples were post-treated by washing the AL4083 PEDOT:PSS using the named solvent. Though the samples show almost similar amount of absorbance over the visible spectrum in Figure 4.1(a), the control sample showed a higher

absorbance compared to others. The increased absorbance indicates improved crystallinity of the perovskite crystal formed on the pristine AL4083 PEDOT:PSS, an effect which was also observed in the PL spectra (see Figure 4.1(b)). The high intensity and slightly red-shifted PL of the pristine AL4083/CsMAFA indicates larger crystal domains and less nonradiative surface recombination due presence of grain boundaries [4]. Chou et al noted in their research that the treatment of the PEDOT:PSS layer increases its surface roughness [84] which might be a poor substrate for the perovskite crystallization compared to the pristine AL4083. AL4083 was with EG showed the lowest PL intensity compared to solvent as it induces more conformational change to the PEDOT chain from the coil to extended coil or linear structure [87a] thus more impact on the crystallization of the CsMAFA layer.

Figure 4.2 below shows the absorbance spectra and PL spectra of the CsMAFA perovskite on the treated PH PEDOT:PSS layer. Pristine PH PEDOT:PSS shows slightly higher absorption over the visible light spectrum compared to the post-treated PEDOT layers (see Figure 4.2a). The PEDOT treated with DMSO showed the highest PL intensity and is slightly red-shifted compared to others (see Figure 4.2a and b) indicating better crystallinity. In Figure 4.3 a, there was no noticeable change in the absorption between the CsMAFA on the pristine and treated PH PEDOT:PSS. Rather the PEDOT treated with DMSO showed higher PL intensity (see Figure 4.3b) compared to others indicating decreased nonradiative surface recombination due to better crystal domains interaction fewer grain boundaries.
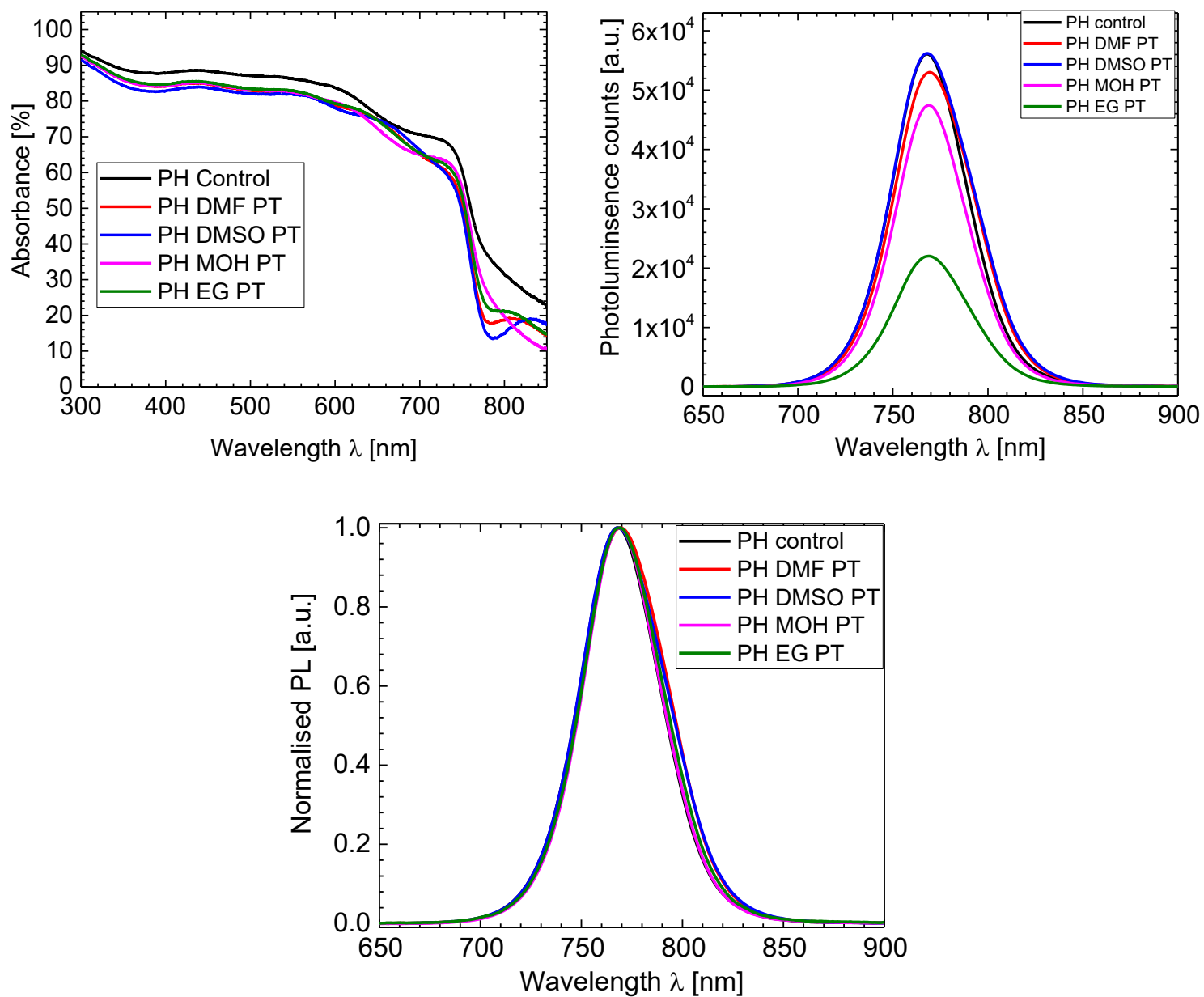
Figure 4.2: (a)Absorbance,(b) PL and (c) Normalised PL spectra of CsMAFA on PH
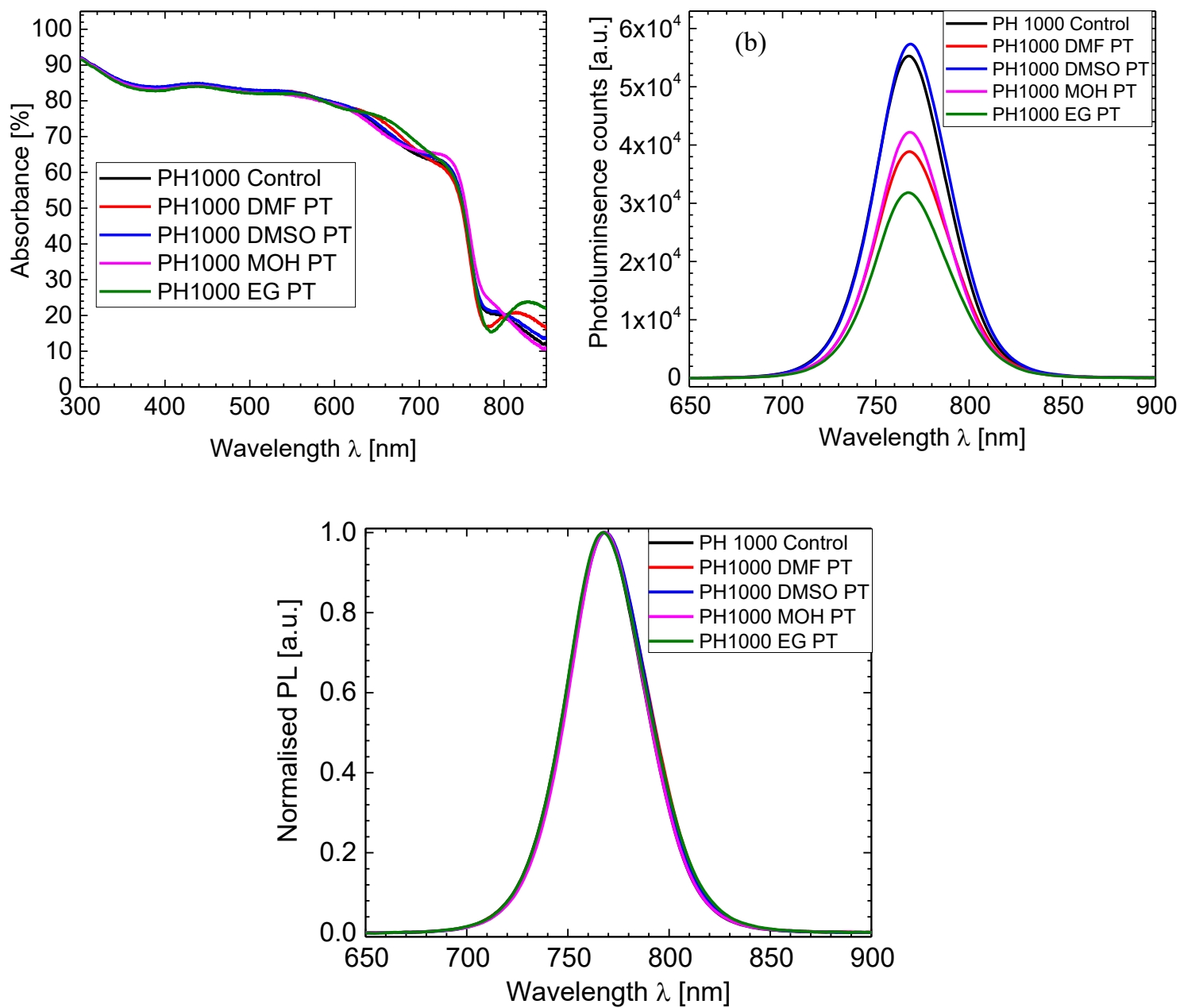
Figure 4.3: (a)Absorbance, (b)PL and (c)Normalized PL spectra of CsMAFA on PH1000.
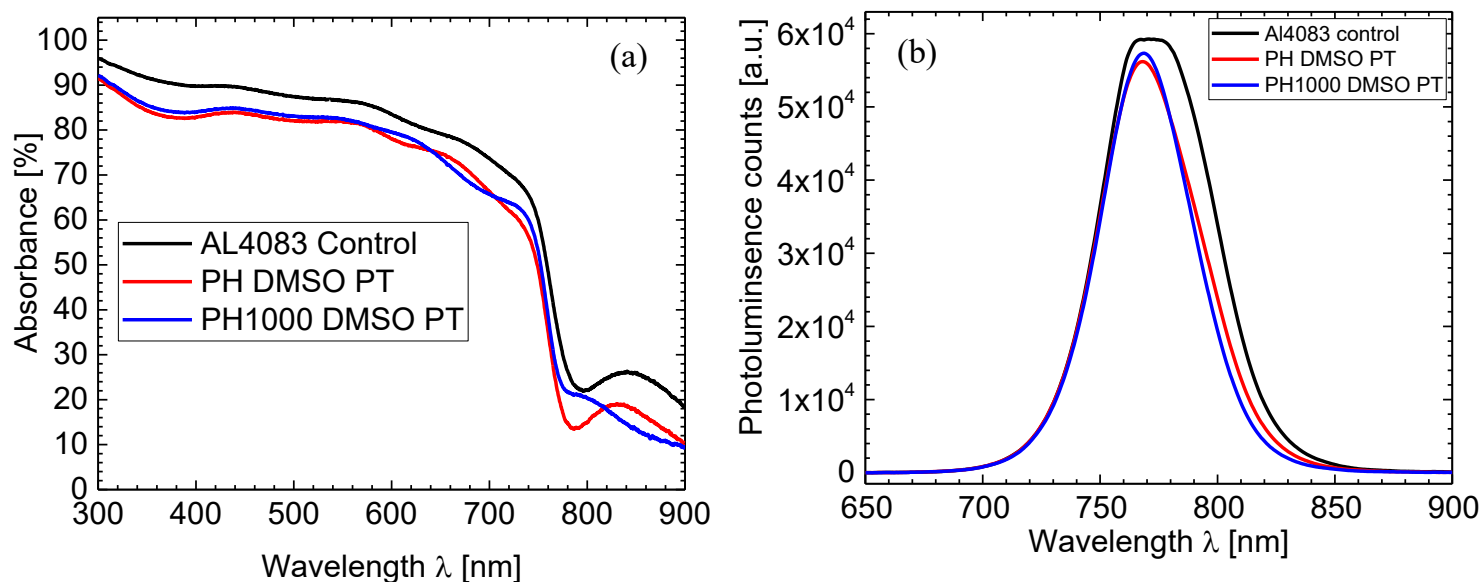
Figure 4.4: (a)Absorbance and (b)PL spectra of best CsMAFA films across the different PEDOTs.

Figure 4.4 shows the comparison of the best CsMAFA films across the three PEDOT:PSS. It can be deduced that pristine AL4083 PEDOT:PSS layer gives the champion film with better crystallinity compared to PH and PH1000 treated with DMSO.

The PEDOT:PSS layer is not solely treated to improve the crystallinity of the perovskite layer. Asides the interfacial morphology of PEDOT:PSS layer with the active layer, hole conductivity, and band alignment are another important properties for the PEDOT:PSS layer treatment. Unfortunately, the effect of the treatment these properties cannot be ascertained using the UV-vis spectroscopy and photoluminescence measurements. Hence, the effect of the PEDOT:PSS treatment on solar cell parameters would be investigated

4.2 Comparing the effect PEDOT treatment on CsMAFA, One MAPI, and Two Step MAPI.
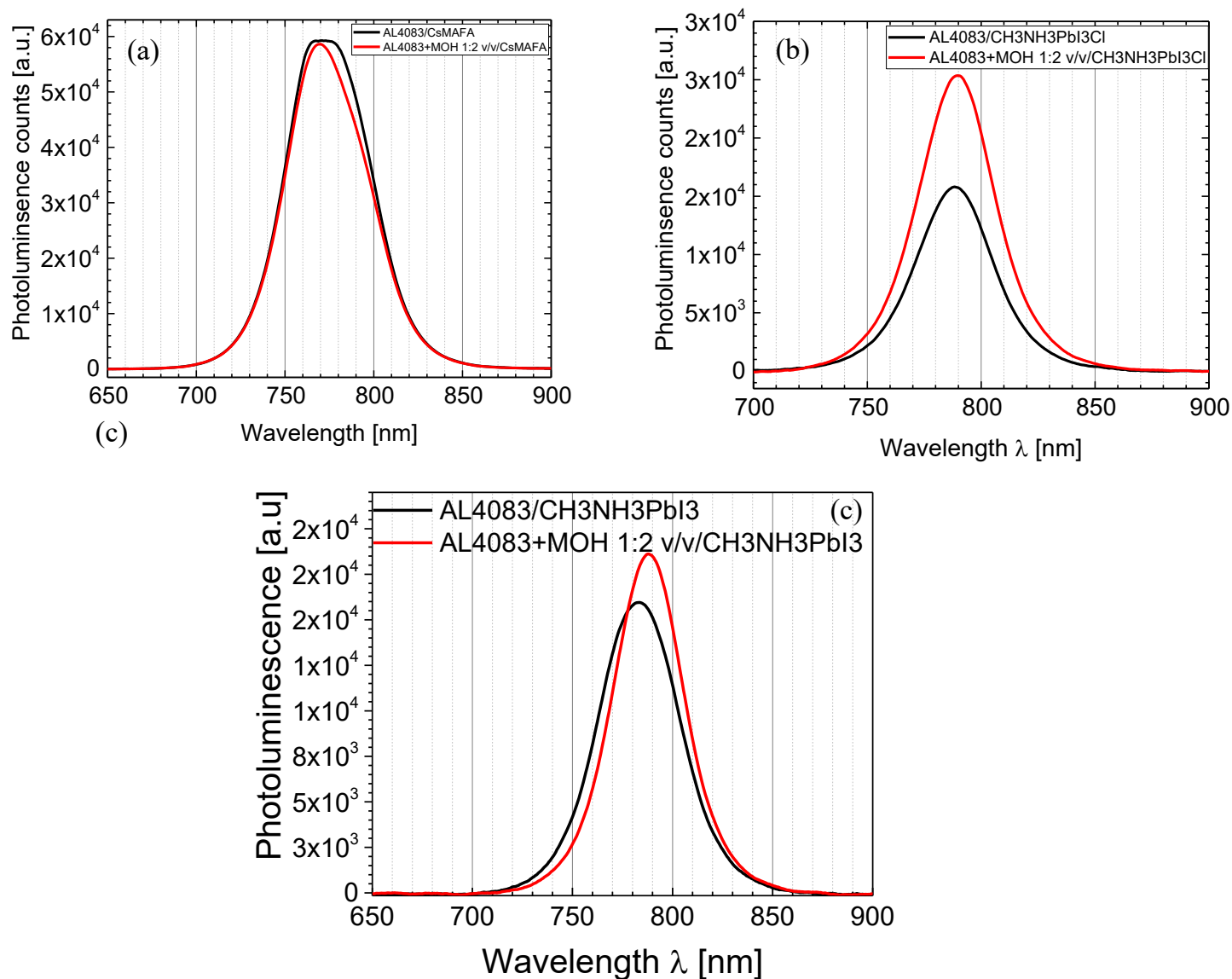
Figure 4.5:PL spectra of (a)CsMAFA, (b)One step MAPI, (c)two-step MAPI respectively.

In this experiment, we investigated the effect of PEDOT:PSS treatment on perovskites achieved through different synthesis route. AL4083 and AL4083+MOH 1:2 v/v doped with methanol at the ratio of 1:2 (without any post-treatment) were used in this experiment. The

PL curves (see Figure 4.5a) indicates that while pristine Al4083 substrate yields CsMAFA perovskite with better crystallinity, Al4083 doped with MOH improved the crystallinity of the one step and two step MAPI which is similar to the result obtained by Huang et al[83]. The impact of PEDOT:PSS treatment on the crystallinity is dependent on the perovskite composition and the fabrication route.

4.3 Methylamine Gas treatment of the active layer.

Solution-processed perovskite films unvaryingly contain defects, such as voids and pinholes. This experiment is the post-processing morphology-reconstruction of perovskite film to heal inherent defects and also improve the crystal quality and size. In this study, one step MAPI films were treated with methylamine gas for different durations. The MAPI perovskite films used were prepared 6 days prior to the treatment and by the 6th day, the films emit very weak PL signals with show lead iodide peaks (see Figure 4.7). The presence of the lead iodide peaks indicates degradation or poor film formation [108].

Methylamine gas induced healing was observed as the film turns darker and appear more compact (see Figure 4.6) which in concord with the observation of Zhou et al [104]. Figure 4.6(a-f) shows the photographic images of the MAPI films before and after CH_3NH_2 treatment. It was observed that the films got darker as the duration of treatment increases and same with the number of visible pinholes

Before   After

ZTI064(annealed for 2 min)

ZTI063(annealed for 5 min)

ZTI065(annealed for 10 min)
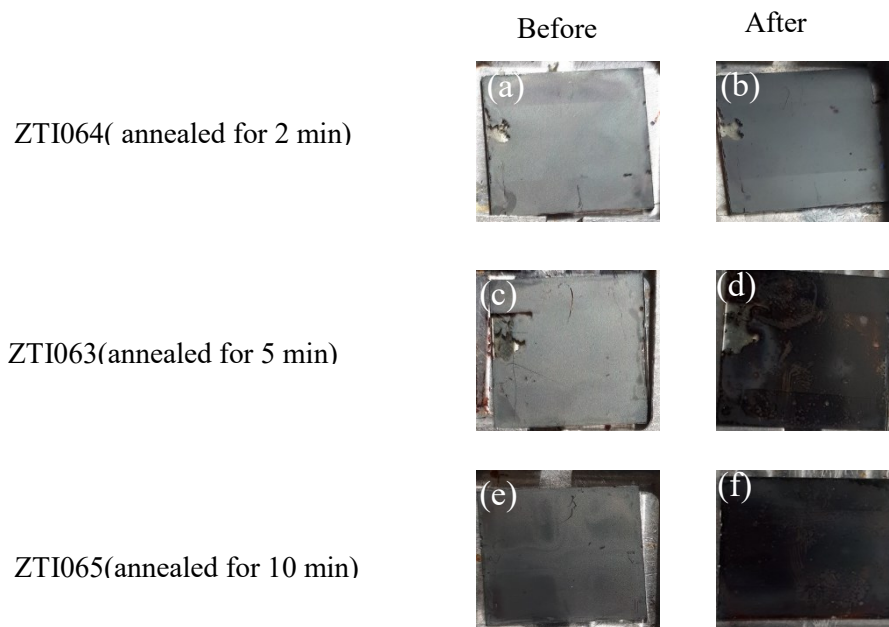
Figure 4.6: MAPI films before and after annealing.
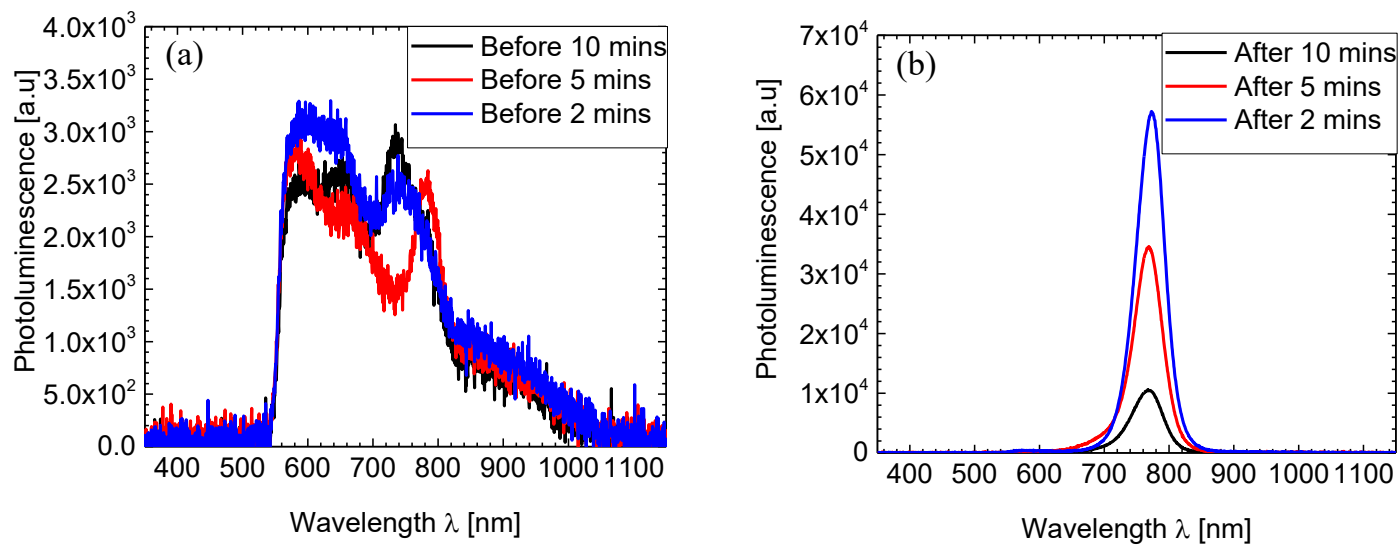
Figure 4.7: The PL of the MAPI films before and after Methylamine gas treatment.

For the film treated for 2 min (see Figure 4.6a and b), healed pinholes were observed from physical inspection. As the time of treatment increased to 5 min though the films got darker, there was an increase in the quantity and size of pinholes which is might be caused by the contraction of the liquid phase MAPI.

This contraction is due variation in the surface energy of the substrate on which the perovskite was deposited. This contraction had more effect as the time of treatment increased since the liquefied perovskite had more time to 'flow'. The defect healing of the treatment of the MAPI films was also observed in more than 20-fold increase in measured PL signal after the treatment which also shows no peak of lead iodide (see Figure 4.7). The increase in the PL intensity and elimination of the lead iodide peak is indicative of crystallinity and texture in the healed film, which is highly desirable for PSCs application [104]. The increase of pinholes with increasing duration of treatment had a detrimental impact on the PL (see Figure 4.7b).
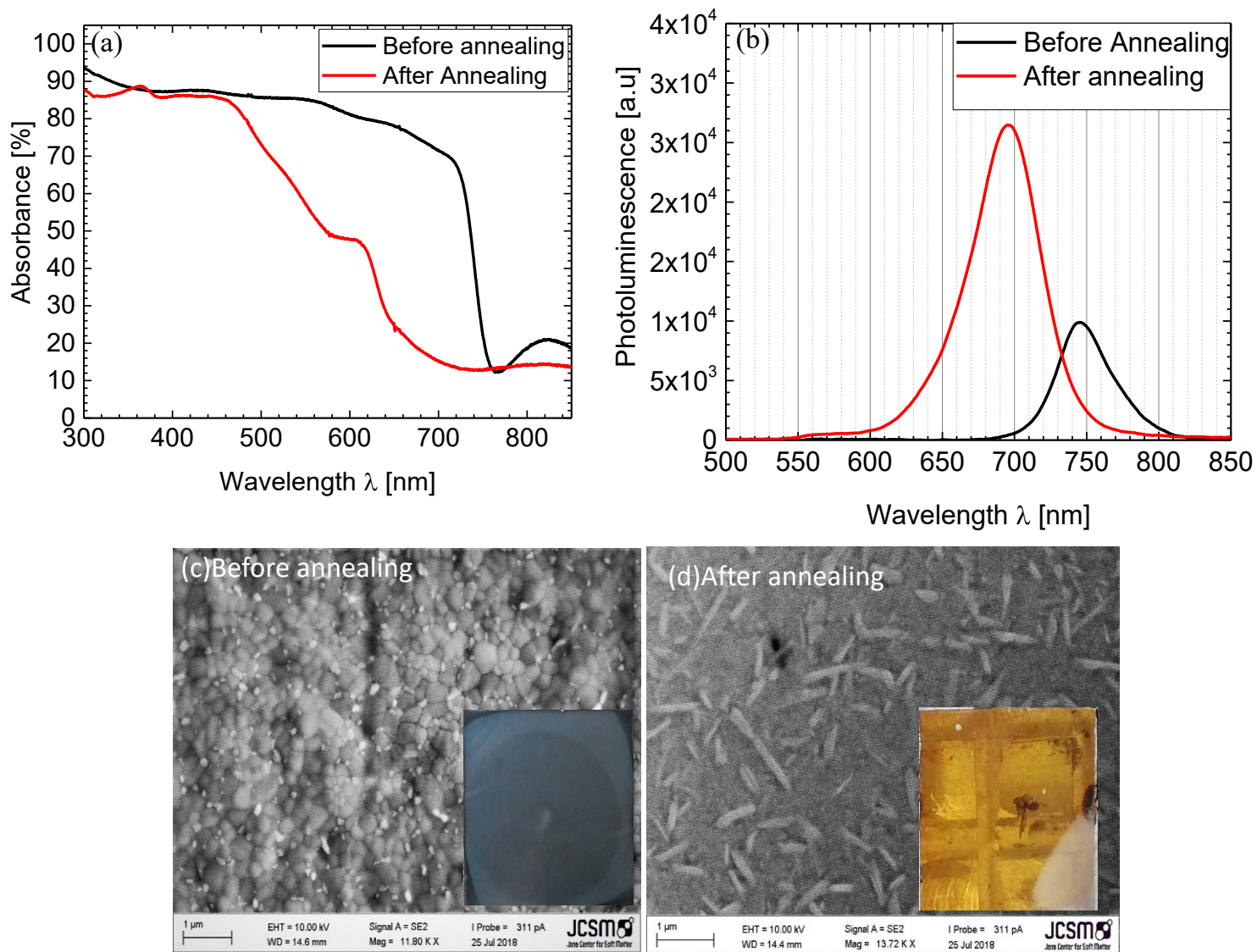
Figure 4.8: (a)Absorbance, (b) PL, (c,d) SEM images (inserts are the picture) of

CsMAFA films before and after Methylamine gas treatment.

The methylamine gas had a different impact when applied on CsMAFA thin film compared to the MAPI film. As can be seen in the *Figure 4.8*c and d, the dark CsMAFA film turned yellow after the gas treatment. The UV-vis spectroscopy result (see *Figure 4.8*a) shows a shift in band edge from ca. 1.59eV before treatment to ca. 1.87eV after treatment. Furthermore, the after treated PL measurement is blue shifted with a high intensity(see *Figure 4.8*b). These results are indicative of the transformation of the dark CsMAFA perovskite (α-phase) to its yellow photoinactive hexagonal polymorph δ-phase [29]. Since the gas treatment was carried out room temperature, thus it favored crystallization of the more room temperature stable yellow polymorph phase [109]. The yellow photoinactive δ-phase exists as a 1D chain like structure with hexagonal symmetry thus the needle-like observed in the SEM image(see *Figure 4.8*d)[109].

4.4 Solvent Vapor Treatment of the active layer.

DMF solvent vapor annealing was carried out on the CsMAFA perovskite layer with the aim of improving the crystal growth. It was observed that the solvent vapor annealing was more suitable for improving the crystallinity of the CsMAFA perovskite compared to methylamine gas treatment. Phase transformation was not observed after the treatment. Figure 4.9 (a) shows increased absorption for the solvent annealed (SA) sample compared to the sample that underwent only thermal annealing(TA). The SA showed a red-shifted PL peak at 750nm compared to the 745nm peak of the TA sample (see Figure 4.9 b). These results are indicative of improved crystallinity and larger crystal domains of the SA sample

which will be beneficial in improving the efficiency of the solar. The SEM images (see

Figure 4.9c and d) confirm increased crystal domain sizes.
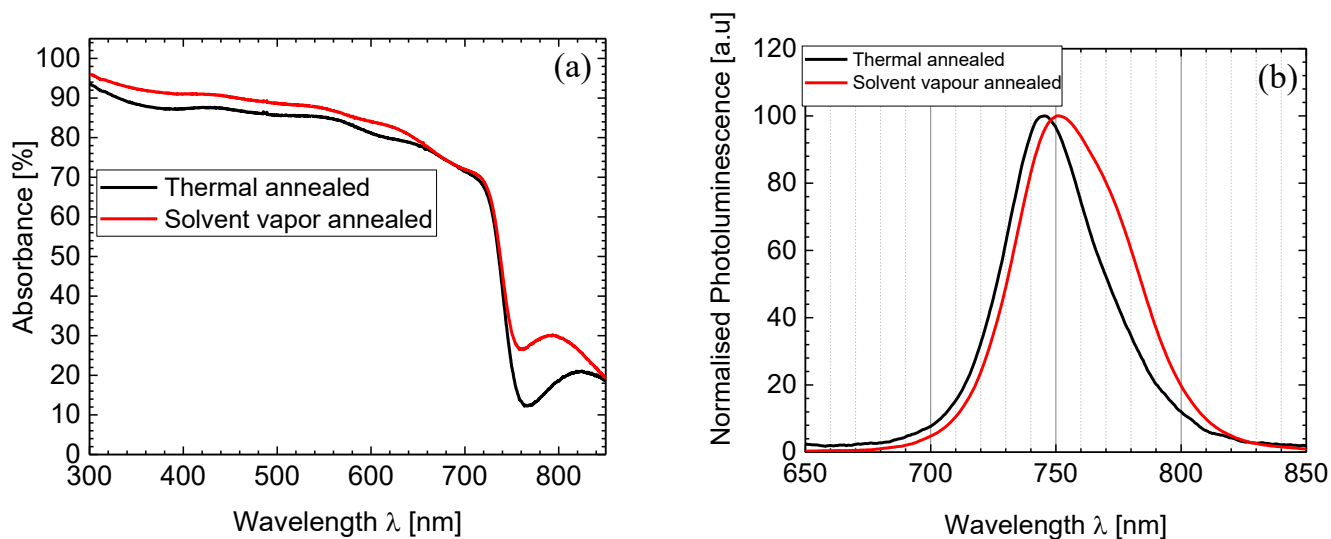
Figure 4.9: (a)Absorbance, (b) PL, (c,d) SEM images (inserts are the picture) of CsMAFA films before and after Solvent vapor treatment.

4.5 PCBM Layer Optimization with 2-step MAPI

The aim of this experiment is to determine the optimum PCBM layer thickness for our solar cells. The optimum should be thick enough to give uniform coverage over the active layer whilst protecting the active layer from coming in contact with the Aluminum electrode. And also should be thin enough for improved charge transport. Prior to this experiment, a pre-test was carried out to determine the effect of PCBM annealing our solar cells adopting the method by Shao et al[36]. Though the entire batch of solar cells shows very poor performance, we observed that the annealed samples to some extent arrested aluminum ingress into the perovskite layer compared to the non-annealed samples. So we adopted PCBM annealing for the rest of the optimization process.

In this experiment, the thickness of the PCBM layer was varied by varying the spin coating frequency while other processing parameters were fixed. The higher the spin frequency the lower the PCBM thickness. The active layer used was the 2 step MAPI. The solar cells parameters from IV characterization are shown in Table 4.1. Though the performance of the solar cells was poor, it was observed that the PCBM layer spin-coated at 600 rpm gave the highest PCE of 2.11%. This can be attributed to the thicker PCBM layer since it was able to protect the perovskite layer from aluminum ingress during evaporation. Hence the active layer generated more charge carriers as indicated by increased current density compared to the devices coated at a higher frequency.

Table 4.1: JV Parameters of the best cells based on 2-step MAPI.

	PCBM spin frequency	Jsc (mA/cm²)	Voc (mV)	FF (%)	PCE (%)	Rs (Ohm)	Rp (Ohm)	Jmpp (mA/cm²)	Vmpp (mV)	Pmax (mW)
1	600	14.414	402	36	2.11	7	231	9.18	230	0.89
2	800	3.441	881	59	1.8	8	1351	2.5	720	0.76
3	1000	7.322	397	30	0.87	7	189	3.96	220	0.37
4	1500	4.122	595	40	0.98	8	921	2.45	400	0.41
5	3000	5.532	373	30	0.62	9	235	3.1	200	0.26
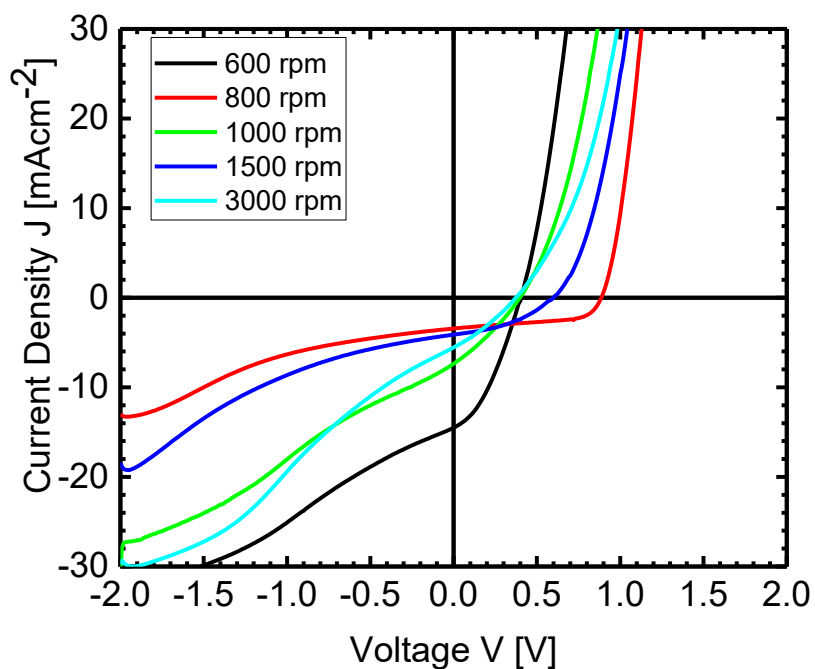
Figure 4.10: JV curve of the best cells based on 2 step MAPI.

The overall shunt resistance (Rp) of the devices were really low indicating high leakage current as shown by the sloping JV curve in the reverse bias of the JV curves of the devices shown in *Figure 4.10.*
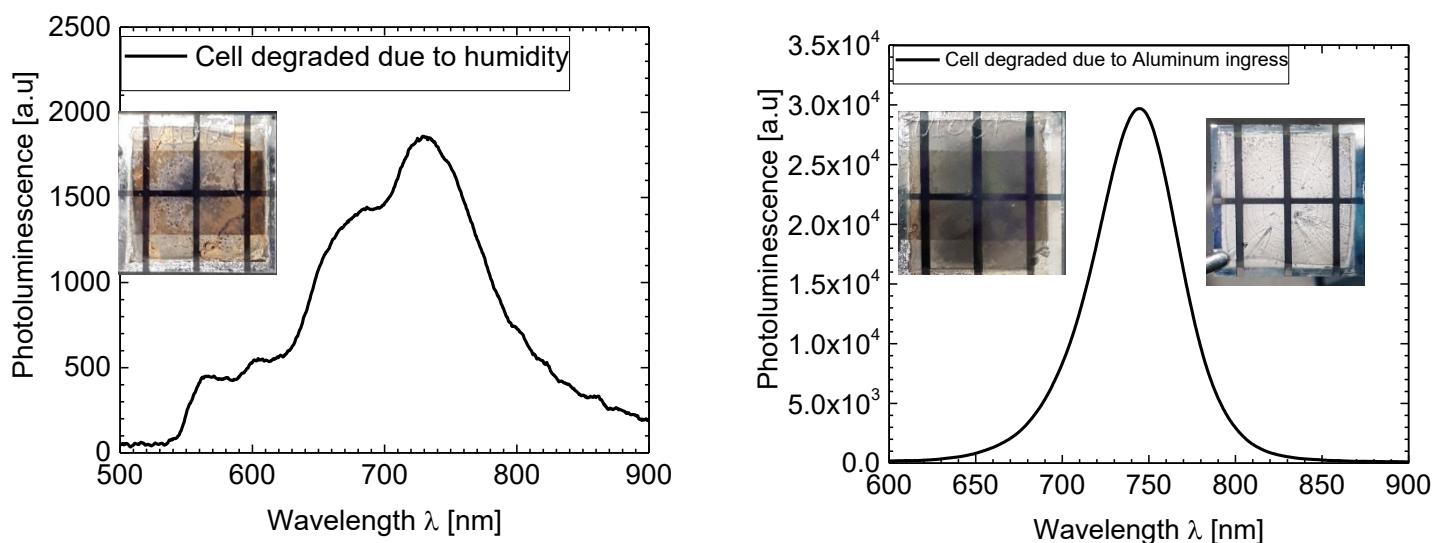
Figure 4.11: PL spectra showing the different effects of different causes of degradation.

In order to ascertain the reason behind the greyish color of the solar cells (see the left insert in Figure 4.11b) as opposed to dark purple, the PL of the cell was measured. It showed a regular the perovskite peak as opposed to a degraded perovskite PL (see Figure 4.11a). This clearly indicates the aluminum ingress during evaporation. Since the perovskite film obtained by the MAPI film is quite rough as observed by visual inspection, hence poor PCBM and TiOx layers coverage which lead to aluminum ingress. Thus the 2 step MAPI was replaced with CsMAFA which give a quite smooth film compared to the MAPI.

4.6 PCBM Layer Optimization with CsMAFA.

This optimization step is similar to the previous one except for the change of the active layer from 2-step MAPI to CsMAFA. Improved JV parameters were observed (Table 4.2). The maximum PCE of 4.16% was obtained for the thickest PCBM layer spun at 600 rpm. The result also shows very low shut resistance all the devices indicating a high leakage current. The fabricated device exhibited quite low V_{OC} values below 0.6 V, this was another contributor to the low fill factor values. The low shunt resistance also had a negative impact on the fill factor.

Table 4.2: JV Parameters of the best cells based on CsMAFA

	PCBM spin frequency	Jsc (mA/cm²)	Voc (mV)	FF (%)	PCE (%)	Rs (Ohm)	Rp (Ohm)	JmPP (mA/cm²)	VmPP (mV)	Pmax (mW)
1	600	15.513	583	46	**4.16**	6	617	11.55	360	1.75
2	800	16.661	349	46	**2.67**	8	341	12.5	213.3	1.12
3	1000	19.993	369	38	**2.82**	8	191	14.84	190	1.18
4	1500	16.671	400	37	**2.47**	7	256	11.59	213.3	1.04
5	2000	18.844	332	37	**2.35**	8	183	13.04	180	0.99
6	3000	14.582	388	40	**2.24**	9	276	9.76	230	0.94
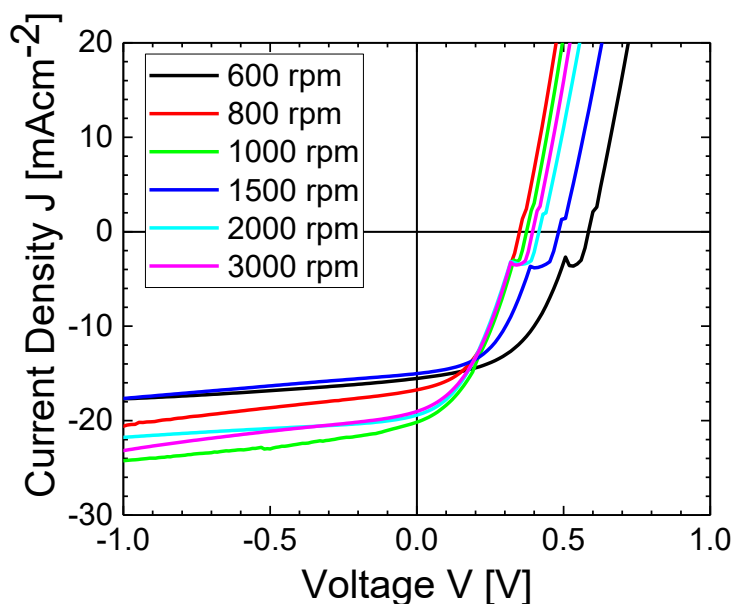
Figure 4.12: JV curve of the best cells based on CsMAFA.

As noted by Wu et al, the limitation on V_{OC} is imposed by parasitic (non-radiative) recombination within the structure, which occurs in the absorber bulk, at the absorber/transport layer interfaces and within the transport layers [107]. Hoppe et al further explained that loss of V_{OC} may arise from the aluminum electrodes, which can form a thin oxide layer at the interface to the organic materials (in our case PCBM) resulting in possible changes in the effective work function [37]. This might due to the poor film morphology of TiO_X layer, the thin inorganic buffer layer which prevents the direct contact between the PCBM layer and aluminum electrode. The poor film morphology of the TiO_X was due to its processing (static spin coating). It was observed in a subsequent experiment that dynamic spin coating rather than a static spin coating of the TiO_X yielded a better film morphology thus improved V_{OC}.

4.7 **Investigation of AL4083 PEDOT:PSS Treatment on solar cell parameters**.

Here the effect of PEDOT:PSS treatment was investigated. CsMAFA was the active layer used in this experiment. With regards to the previous PCBM optimization experiments outcomes, a thicker PCBM layer was achieved by spin coating 40mg/mL of PCBM in DCB at 1000 rpm.

Table 4.3: Parameters of the best cells showing the effect of PEDOT:PSS treatment.

	Al4083	Post treatment	Jsc (mA /cm²)	Voc (mV)	FF (%)	PCE (%)	Rs (Ohm)	Rp (Ohm)	JmPP (mA/cm²)	VmPP (mV)	Pmax (mW)
1	PEDOT:PSS	None	26.457	862	59	13.49	7	1068	21.4	630	5.66
2	PEDOT:PSS +MeOH 1:2 v/v	None	19.168	959	63	11.58	6	2540	15.65	740	4.86
3	PEDOT:PSS	DMF	24.857	371	41	3.77	9	207	17.15	220	1.58
4	PEDOT:PSS	DMSO	27.573	535	51	7.49	7	422	20.81	360	3.15
5	PEDOT:PSS	EG	25.968	763	51	10.07	5	700	20.15	500	4.23
6	PEDOT:PSS	MeOH	20.255	646	51	6.62	5	583	15.39	430	2.78
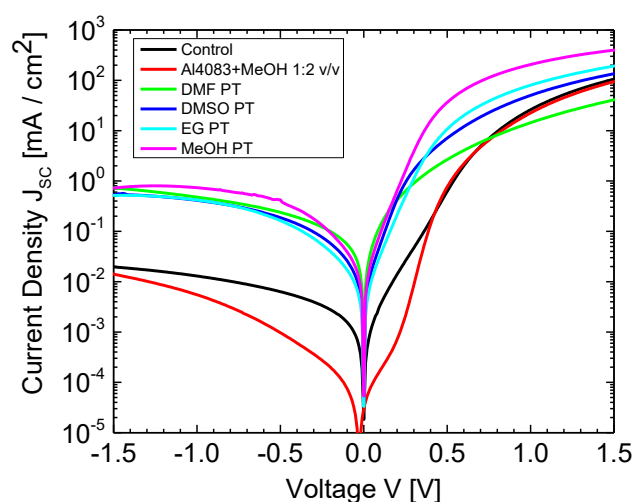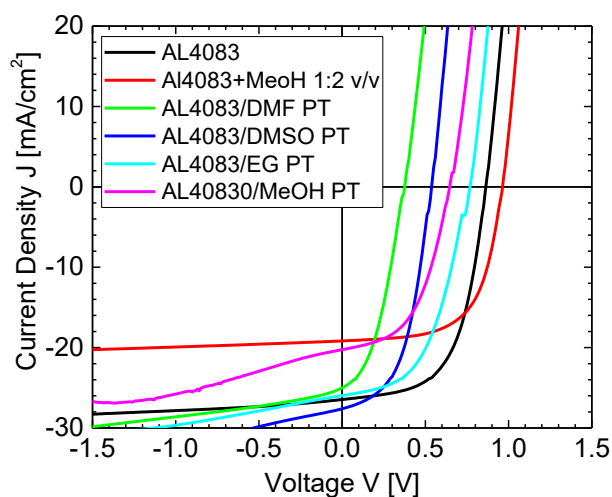
Figure 4.13: Light and dark JV curve of the best cells showing the effect of PEDOT:PSS treatment

Table 1.1 shows the IV parameters of the best cells while in Figure 4.13 the light and dark JV curves were presented. The untreated Al4083 layer give the cell with highest PCE of 13.49% with current density of 26.5 mA/cm^2 and V_{OC} of 0.86 V. The improved solar cell parameters can be as a result of improved crystallinity of CsMAFA active layer as indicated by increased intensity as and slightly red-shifted PL (see Figure 4.1a and b). This indicates fewer recombination sites within the active layer. The V_{OC}, FF, and R_{sh} are relatively low, this is indicative of non-ideal contacts or misalignment of the energy bands of the active layer and charge transport layer [37].

The device with the Al4083 PEDOT:PSS layer doped 1:2 v/v of methanol, produced the cell with the highest FF and V_{OC} values of 63% and 0.959 V with improved efficiency of approximately 11.6%. These improved parameters can be attributed to the enhanced hole extraction at the HTL-active layer interface as observed by Tan et al in their PEDOT:PSS treated by methanol experiment on organic solar cell. The enhanced hole extraction rate at the active layer/HTL interface will reduce/avoid the accumulation of holes near the anode, therefore preventing the screening of the internal field as well as suppressing bimolecular recombination. The depletion of holes near the anode via improved extraction rates also enhances diffusive transport by establishing a hole density gradient. The reduction of charge recombination and improved transport enable higher photocurrent collection yield across the forward bias regime and manifests itself as an improved fill factor and improved power conversion efficiency for the solar cell [110].

It was also observed from Table 4.3 that DMSO post-treated of AL4083 PEDOT:PSS yielded a very high J_{SC} of 27.573 mA/cm^2 which indicates an increase in hole conductivity. A similar observation was made by Huang et al, where almost a 40% increase in the J_{SC} was observed after AL4083 was treated with DMSO [83]. This increase in hole conductivity can be attributed to the coarse topology of DMSO treated PEDOT:PSS has been ascribed to the formation of desirable PEDOT-rich bead- like aggregates, which are more conductive and favor hole transport at the interface. Furthermore, the moderately rough interface can be beneficial towards improving the actual contact area between the HTL and the active layer [83-84].

Surprisingly, the PEDOT:PSS treated EG showed higher performance compared to DMF, DMSO, and methanol post-treated devices. With respect to Figure 4.1a, the PL intensity for the EG treated layer was the lowest. Hence, the increase in the can be attributed to band alignment of the work function PEDOT layer treated with EG with the valance band of the active layer. In conclusion, more experiments and measurements (such AFM for surface roughness, work function measurements) would be needed to further understand the impact of PEDOT:PSS treatment and further optimization. Though the performance of CsMAFA inverted devices with the exact layer materials used in this thesis are not yet in the literature, it is possible to attain close to the best for perovskite solar cells(23.3% [11]) using our structure and materials.

Chapter 5

Summary and Outlook

Organic-inorganic halide perovskite materials have the potential to disrupt the current photovoltaics landscape. Organic-inorganic halide perovskite materials are synthesized from cheap and abundant. They also possess unique optoelectronic and physical properties thus used for highly efficient, cheap and facile to fabricate solar cells.

In this thesis, a layer by layer approach of optimizing inverted organic-inorganic halide perovskite solar cell using PEDOT:PSS and PCBM as HTL and ETL respectively was carried out. The effects of solvent post-treatment of PEDOT:PSS (AL4083, PH, and PH1000) on the crystallinity of the mixed cation and anion perovskite were investigated. Through which we found that untreated AL4083 PEDOT:PSS yielded CsMAFA with improved crystallinity for the AL4083 batch while DMSO treated PH and PH1000 gave CsMAFA with better crystallinity in their separate batches. Improved crystal growth of the CsMAFA perovskite was achieved via solvent vapor annealing. Methylamine gas annealing found to be unsuitable as it leads to the formation of photoinactive yellow phase. Optimization of the PCBM layer was also achieved. Effect of post-treatment of Al4083 PEDOT:PSS on solar cell parameters was investigated and a maximum of 13.49% PCE was achieved.

Further research is required to achieve the reproducibility and encapsulation of the optimized solar cell for subsequent stability investigations. Also a further study on the effects of the post-treatment of PH and PH1000 PEDOT:PSS on the solar cell parameters is suggested.

References

[1]   I. E. Agency, in *World Energy Outlook* (Ed.: I. E. Agency), **2017**, p. 144.
[2]   UNEP, United Nations Environment Programme, Nairobi, Kenya, **2017**.
[3]   E. Becquerel, *Compt. rend.* **1839**, *9*, 561.
[4]   N. Marinova, S. Valero, J. L. Delgado, *Journal of colloid and interface science* **2017**, *488*, 373-389.
[5]   J. Bisquert, *The Physics of Solar Cells_ Perovskites, Organics, and Photovoltaic Fundamentals*, CRC Press, Taylor & Francis Group, Boca Raton, FL, **2018**.
[6]   M. Stringer, The University of Sheffield (EPSRC Centre for Doctoral Training, 'New and Sustainable Photovoltaics), **2015**.
[7]   M. Ulkuniemi, Master's thesis thesis, University of Oulu
[8]   D. M. Bagnall, M. Boreland, *Energy Policy* **2008**, *36*, 4390-4396.
[9]   S. A. G. F. C. Krebs, PhD thesis, DTU (Roskilde: Risø National Laboratory for Sustainable Energy), **2010**.
[10]   A. Kojima, K. Teshima, Y. Shirai, T. Miyasaka, *Journal of the American Chemical Society* **2009**, *131*, 6050-6051.
[11]   NREL*, Vol. 2018*, **2018**.
[12]   Y. Chen, M. He, J. Peng, Y. Sun, Z. Liang, *Advanced Science* **2016**, *3*, 1500392.
[13]   B. O'Regan, M. Grätzel, *Nature* **1991**, *353*, 737.
[14]   H. S. Kim, C. R. Lee, J. H. Im, K. B. Lee, T. Moehl, A. Marchioro, S. J. Moon, R. Humphry-Baker, J. H. Yum, J. E. Moser, M. Gratzel, N. G. Park, *Scientific reports* **2012**, *2*, 591.
[15]   M. M. Lee, J. Teuscher, T. Miyasaka, T. N. Murakami, H. J. Snaith, *Science* **2012**, *338*, 643.
[16]   M. Liu, M. B. Johnston, H. J. Snaith, *Nature* **2013**, *501*, 395.
[17]   S. Brittman, G. W. Adhyaksa, E. C. Garnett, *MRS communications* **2015**, *5*, 7-26.
[18]   Q. Chen, N. De Marco, Y. Yang, T.-B. Song, C.-C. Chen, H. Zhao, Z. Hong, H. Zhou, Y. Yang, *Nano Today* **2015**, *10*, 355-396.
[19]   C. Li, X. Lu, W. Ding, L. Feng, Y. Gao, Z. Guo, *Acta Crystallographica Section B* **2008**, *64*, 702-707.
[20]   J.-P. Correa-Baena, A. Abate, M. Saliba, W. Tress, T. Jesper Jacobsson, M. Grätzel, A. Hagfeldt, *Energy & Environmental Science* **2017**, *10*, 710-727.
[21]   M. Saliba, T. Matsui, J. Y. Seo, K. Domanski, J. P. Correa-Baena, M. K. Nazeeruddin, S. M. Zakeeruddin, W. Tress, A. Abate, A. Hagfeldt, M. Gratzel, *Energy Environ Sci* **2016**, *9*, 1989-1997.
[22]   N. K. McKinnon, D. C. Reeves, M. H. Akabas, *The Journal of general physiology* **2011**, *138*, 453-466.
[23]   Y. Dang, Y. Liu, Y. Sun, D. Yuan, X. Liu, W. Lu, G. Liu, H. Xia, X. Tao, *CrystEngComm* **2015**, *17*, 665-670.
[24]   T. Baikie, Y. Fang, J. M. Kadro, M. Schreyer, F. Wei, S. G. Mhaisalkar, M. Graetzel, T. J. White, *Journal of Materials Chemistry A* **2013**, *1*, 5628.
[25]   T. J. Jacobsson, W. Tress, J.-P. Correa-Baena, T. Edvinsson, A. Hagfeldt, *The Journal of Physical Chemistry C* **2016**, *120*, 11382-11393.

[26] aT. J. Jacobsson, L. J. Schwan, M. Ottosson, A. Hagfeldt, T. Edvinsson, *Inorganic chemistry* **2015**, *54*, 10678-10685; bC. C. Stoumpos, C. D. Malliakas, M. G. Kanatzidis, *Inorganic chemistry* **2013**, *52*, 9019-9038.

[27] aD. M. Jang, K. Park, D. H. Kim, J. Park, F. Shojaei, H. S. Kang, J. P. Ahn, J. W. Lee, J. K. Song, *Nano letters* **2015**, *15*, 5191-5199; bJ. W. Lee, D. J. Seol, A. N. Cho, N. G. Park, *Advanced materials* **2014**, *26*, 4991-4998; cM. R. Filip, G. E. Eperon, H. J. Snaith, F. Giustino, *Nature communications* **2014**, *5*, 5757.

[28] M. T. Weller, O. J. Weber, J. M. Frost, A. Walsh, *The Journal of Physical Chemistry Letters* **2015**, *6*, 3209-3212.

[29] T. Jesper Jacobsson, J.-P. Correa-Baena, M. Pazoki, M. Saliba, K. Schenk, M. Grätzel, A. Hagfeldt, *Energy & Environmental Science* **2016**, *9*, 1706-1724.

[30] K. Zheng, Q. Zhu, M. Abdellah, M. E. Messing, W. Zhang, A. Generalov, Y. Niu, L. Ribaud, S. E. Canton, T. Pullerits, *J Phys Chem Lett* **2015**, *6*, 2969-2975.

[31] S. D. Stranks, G. E. Eperon, G. Grancini, C. Menelaou, M. J. P. Alcocer, T. Leijtens, L. M. Herz, A. Petrozza, H. J. Snaith, *Science* **2013**, *342*, 341.

[32] T. Leijtens, S. D. Stranks, G. E. Eperon, R. Lindblad, E. M. J. Johansson, I. J. McPherson, H. Rensmo, J. M. Ball, M. M. Lee, H. J. Snaith, *ACS Nano* **2014**, *8*, 7147-7155.

[33] C. Wehrenfennig, G. E. Eperon, M. B. Johnston, H. J. Snaith, L. M. Herz, *Advanced materials* **2013**, *26*, 1584-1589.

[34] M. Konstantakou, T. Stergiopoulos, *Journal of Materials Chemistry A* **2017**, *5*, 11518-11549.

[35] C. Jiang, S. L. Lim, W. P. Goh, F. X. Wei, J. Zhang, *ACS Applied Materials & Interfaces* **2015**, *7*, 24726-24732.

[36] Y. Shao, Z. Xiao, C. Bi, Y. Yuan, J. Huang, *Nature communications* **2014**, *5*, 5784.

[37] H. Hoppe, N. S. Sariciftci, **2007**, 1-86.

[38] C. Deibel, V. Dyakonov, *Reports on Progress in Physics* **2010**, *73*, 096401.

[39] W. Shockley, H. J. Queisser, *Journal of applied physics* **1961**, *32*, 510-519.

[40] N. K. Elumalai, A. Uddin, *Energy Environ. Sci.* **2016**, *9*, 391-410.

[41] M. Green, *Third Generation Photovoltaics; Advanced Solar Energy Conversion*, 1 ed., Springer-Verlag Berlin Heidelberg, **2003**.

[42] M. Ratner, *Physics Today* **2004**, *57*, 71-72.

[43] J. H. Heo, D. H. Song, H. J. Han, S. Y. Kim, J. H. Kim, D. Kim, H. W. Shin, T. K. Ahn, C. Wolf, T. W. Lee, S. H. Im, *Advanced materials* **2015**, *27*, 3424-3430.

[44] UNDP, United Nations Development Programme and World Energy Council, **2000**.

[45] IEA, International Energy Agency, **2016**.

[46] U. S. E. I. Administration, **2018**.

[47] D. Zhou, T. Zhou, Y. Tian, X. Zhu, Y. Tu, *Journal of Nanomaterials* **2018**, *2018*, 1-15.

[48] J. F. Iannello, Master of Science thesis, Rowan University **2018**.

[49] K. Yoshikawa, W. Yoshida, T. Irie, H. Kawasaki, K. Konishi, H. Ishibashi, T. Asatani, D. Adachi, M. Kanematsu, H. Uzu, K. Yamamoto, *Solar Energy Materials and Solar Cells* **2017**, *173*, 37-42.

[50] M. A. Green, A. Ho-Baillie, H. J. Snaith, *Nature Photonics* **2014**, *8*, 506-514.

[51] A. Marchioro, J. Teuscher, D. Friedrich, M. Kunst, R. van de Krol, T. Moehl, M. Grätzel, J.-E. Moser, *Nature Photonics* **2014**, *8*, 250-255.

[52]   C. Roldán-Carmona, P. Gratia, I. Zimmermann, G. Grancini, P. Gao, M. Graetzel, M. K. Nazeeruddin, *Energy & Environmental Science* **2015**, *8*, 3550-3556.

[53]   G. E. Eperon, S. D. Stranks, C. Menelaou, M. B. Johnston, L. M. Herz, H. J. Snaith, *Energy & Environmental Science* **2014**, *7*, 982.

[54]   N. J. Jeon, J. H. Noh, W. S. Yang, Y. C. Kim, S. Ryu, J. Seo, S. I. Seok, *Nature* **2015**, *517*, 476-480.

[55]   M. Saliba, J.-P. Correa-Baena, C. M. Wolff, M. Stolterfoht, N. Phung, S. Albrecht, D. Neher, A. Abate, *Chemistry of Materials* **2018**.

[56]   J. Y. Jeng, Y. F. Chiang, M. H. Lee, S. R. Peng, T. F. Guo, P. Chen, T. C. Wen, *Advanced materials* **2013**, *25*, 3727-3732.

[57]   S. Sun, T. Salim, N. Mathews, M. Duchamp, C. Boothroyd, G. Xing, T. C. Sum, Y. M. Lam, *Energy Environ. Sci.* **2014**, *7*, 399-407.

[58]   J. You, Z. Hong, Y. Yang, Q. Chen, M. Cai, T.-B. Song, C.-C. Chen, S. Lu, Y. Liu, H. Zhou, Y. Yang, *ACS Nano* **2014**, *8*, 1674-1680.

[59]   P. Docampo, J. M. Ball, M. Darwich, G. E. Eperon, H. J. Snaith, *Nature communications* **2013**, *4*, 2761.

[60]   J. Seo, S. Park, Y. Chan Kim, N. J. Jeon, J. H. Noh, S. C. Yoon, S. I. Seok, *Energy Environ. Sci.* **2014**, *7*, 2642-2646.

[61]   J. You, Y. Yang, Z. Hong, T.-B. Song, L. Meng, Y. Liu, C. Jiang, H. Zhou, W.-H. Chang, G. Li, Y. Yang, *Applied Physics Letters* **2014**, *105*, 183902.

[62]   W. Nie, H. Tsai, R. Asadpour, J.-C. Blancon, A. J. Neukirch, G. Gupta, J. J. Crochet, M. Chhowalla, S. Tretiak, M. A. Alam, H.-L. Wang, A. D. Mohite, *Science* **2015**, *347*, 522.

[63]   J. H. Heo, H. J. Han, D. Kim, T. K. Ahn, S. H. Im, *Energy & Environmental Science* **2015**, *8*, 1602-1608.

[64]   O. Malinkiewicz, A. Yella, Y. H. Lee, G. M. Espallargas, M. Graetzel, M. K. Nazeeruddin, H. J. Bolink, *Nature Photonics* **2013**, *8*, 128.

[65]   Q. Lin, A. Armin, R. C. R. Nagiri, P. L. Burn, P. Meredith, *Nature Photonics* **2014**, *9*, 106-112.

[66]   C. Bi, Q. Wang, Y. Shao, Y. Yuan, Z. Xiao, J. Huang, *Nature communications* **2015**, *6*, 7747.

[67]   P.-W. Liang, C.-C. Chueh, S. T. Williams, A. K. Y. Jen, *Advanced Energy Materials* **2015**, *5*, 1402321.

[68]   S. Bai, Z. Wu, X. Wu, Y. Jin, N. Zhao, Z. Chen, Q. Mei, X. Wang, Z. Ye, T. Song, R. Liu, S.-t. Lee, B. Sun, *Nano Research* **2014**, *7*, 1749-1758.

[69]   L. Q. Zhang, X. W. Zhang, Z. G. Yin, Q. Jiang, X. Liu, J. H. Meng, Y. J. Zhao, H. L. Wang, *Journal of Materials Chemistry A* **2015**, *3*, 12133-12138.

[70]   J. Y. Jeng, K. C. Chen, T. Y. Chiang, P. Y. Lin, T. D. Tsai, Y. C. Chang, T. F. Guo, P. Chen, T. C. Wen, Y. J. Hsu, *Advanced materials* **2014**, *26*, 4107-4113.

[71]   aJ. H. Im, I. H. Jang, N. Pellet, M. Gratzel, N. G. Park, *Nature nanotechnology* **2014**, *9*, 927-932; bQ. Chen, H. Zhou, Z. Hong, S. Luo, H. S. Duan, H. H. Wang, Y. Liu, G. Li, Y. Yang, *Journal of the American Chemical Society* **2014**, *136*, 622-625.

[72]   M. R. Leyden, L. K. Ono, S. R. Raga, Y. Kato, S. Wang, Y. Qi, *J. Mater. Chem. A* **2014**, *2*, 18742-18745.

[73]   S. Gamliel, A. Dymshits, S. Aharon, E. Terkieltaub, L. Etgar, *The Journal of Physical Chemistry C* **2015**, *119*, 19722-19728.

[74]   Y. Deng, E. Peng, Y. Shao, Z. Xiao, Q. Dong, J. Huang, *Energy & Environmental Science* **2015**, *8*, 1544-1550.

[75]   K. Hwang, Y. S. Jung, Y. J. Heo, F. H. Scholes, S. E. Watkins, J. Subbiah, D. J. Jones, D. Y. Kim, D. Vak, *Advanced materials* **2015**, *27*, 1241-1247.

[76]   aJ. M. Ball, M. M. Lee, A. Hey, H. J. Snaith, *Energy & Environmental Science* **2013**, *6*, 1739; bH. Zhou, Q. Chen, G. Li, S. Luo, T.-b. Song, H.-S. Duan, Z. Hong, J. You, Y. Liu, Y. Yang, *Science* **2014**, *345*, 542.

[77]   Y. Xu, L. Zhu, J. Shi, S. Lv, X. Xu, J. Xiao, J. Dong, H. Wu, Y. Luo, D. Li, Q. Meng, *ACS Appl Mater Interfaces* **2015**, *7*, 2242-2248.

[78]   J. Burschka, N. Pellet, S. J. Moon, R. Humphry-Baker, P. Gao, M. K. Nazeeruddin, M. Gratzel, *Nature* **2013**, *499*, 316-319.

[79]   aJ. Schlipf, P. Docampo, C. J. Schaffer, V. Korstgens, L. Biessmann, F. Hanusch, N. Giesbrecht, S. Bernstorff, T. Bein, P. Muller-Buschbaum, *J Phys Chem Lett* **2015**, *6*, 1265-1269; bZ. Xiao, Q. Dong, C. Bi, Y. Shao, Y. Yuan, J. Huang, *Advanced materials* **2014**, *26*, 6503-6509; cC.-H. Chiang, Z.-L. Tseng, C.-G. Wu, *J. Mater. Chem. A* **2014**, *2*, 15897-15903.

[80]   aY. Ma, L. Zheng, Y. H. Chung, S. Chu, L. Xiao, Z. Chen, S. Wang, B. Qu, Q. Gong, Z. Wu, X. Hou, *Chemical communications* **2014**, *50*, 12458-12461; bM. Jiang, J. Wu, F. Lan, Q. Tao, D. Gao, G. Li, *Journal of Materials Chemistry A* **2015**, *3*, 963-967.

[81]   C. Bi, Y. Yuan, Y. Fang, J. Huang, *Advanced Energy Materials* **2014**, *5*, 1401616.

[82]   Y. Chen, B. Li, W. Huang, D. Gao, Z. Liang, *Chemical communications* **2015**, *51*, 11997-11999.

[83]   D. Huang, T. Goh, J. Kong, Y. Zheng, S. Zhao, Z. Xu, A. D. Taylor, *Nanoscale* **2017**, *9*, 4236-4243.

[84]   T.-R. Chou, S.-H. Chen, Y.-T. Chiang, Y.-T. Lin, C.-Y. Chao, *Molecular Crystals and Liquid Crystals* **2015**, *612*, 201-210.

[85]   X. Crispin, F. L. E. Jakobsson, A. Crispin, P. C. M. Grim, P. Andersson, A. Volodin, C. van Haesendonck, M. Van der Auweraer, W. R. Salaneck, M. Berggren, *Chemistry of Materials* **2006**, *18*, 4354-4360.

[86]   L. Meng, J. You, T.-F. Guo, Y. Yang, *Accounts of Chemical Research* **2016**, *49*, 155-165.

[87]   aM. O. P. Kara, M. W. Frey, *J. Appl. Polym. Sci.* **2014**, *131*, 8; bM. Yamashita, C. Otani, M. Shimizu, H. Okuzaki, *Applied Physics Letters* **2011**, *99*, 143307.

[88]   C. Badre, L. Marquant, A. M. Alsayed, L. A. Hough, *Advanced Functional Materials* **2012**, *22*, 2723-2727.

[89]   J. Yang, F. Zeng, Z. S. Wang, C. Chen, G. Y. Wang, Y. S. Lin, F. Pan, *Journal of Applied Physics* **2011**, *110*, 114518.

[90]   M. Reyes-Reyes, I. Cruz-Cruz, R. López-Sandoval, *The Journal of Physical Chemistry C* **2010**, *114*, 20220-20224.

[91]   J. Huang, P. F. Miller, J. S. Wilson, A. J. de Mello, J. C. de Mello, D. D. C. Bradley, *Advanced Functional Materials* **2005**, *15*, 290-296.

[92]   K. Sun, Y. Xia, J. Ouyang, *Solar Energy Materials and Solar Cells* **2012**, *97*, 89-96.

[93]   H. Liu, X. Li, L. Zhang, Q. Hong, J. Tang, A. Zhang, C.-Q. Ma, *Organic Electronics* **2017**, *47*, 220-227.

[94]   C. Song, Z. Zhong, Z. Hu, J. Wang, L. Wang, L. Ying, J. Wang, Y. Cao, *Organic Electronics* **2016**, *28*, 252-256.

[95]   Y. Xia, K. Sun, J. Ouyang, *Advanced materials* **2012**, *24*, 2436-2440.
[96]   F. Huang, A. R. Pascoe, W. Q. Wu, Z. Ku, Y. Peng, J. Zhong, R. A. Caruso, Y. B. Cheng, *Advanced materials* **2017**, *29*.
[97]   Y. Bai, Q. Dong, Y. Shao, Y. Deng, Q. Wang, L. Shen, D. Wang, W. Wei, J. Huang, *Nature communications* **2016**, *7*, 12806.
[98]   N. Ahn, D. Y. Son, I. H. Jang, S. M. Kang, M. Choi, N. G. Park, *Journal of the American Chemical Society* **2015**, *137*, 8696-8699.
[99]   B.-E. Cohen, L. Etgar, *Frontiers of Optoelectronics* **2016**, *9*, 44-52.
[100]   aZ. Xiao, Y. Yuan, Q. Wang, Y. Shao, Y. Bai, Y. Deng, Q. Dong, M. Hu, C. Bi, J. Huang, *Materials Science and Engineering: R: Reports* **2016**, *101*, 1-38; bM. Xiao, F. Huang, W. Huang, Y. Dkhissi, Y. Zhu, J. Etheridge, A. Gray-Weale, U. Bach, Y. B. Cheng, L. Spiccia, *Angewandte Chemie* **2014**, *53*, 9898-9903.
[101]   Ossila*, Vol. 2018*.
[102]   D. Wang, Z. Liu, Z. Zhou, H. Zhu, Y. Zhou, C. Huang, Z. Wang, H. Xu, Y. Jin, B. Fan, S. Pang, G. Cui, *Chemistry of Materials* **2014**, *26*, 7145-7150.
[103]   N. Tripathi, M. Yanagida, Y. Shirai, T. Masuda, L. Han, K. Miyano, *Journal of Materials Chemistry A* **2015**, *3*, 12081-12088.
[104]   Z. Zhou, Z. Wang, Y. Zhou, S. Pang, D. Wang, H. Xu, Z. Liu, N. P. Padture, G. Cui, *Angewandte Chemie* **2015**, *54*, 9705-9709.
[105]   aW. Chen, Y. Wu, J. Liu, C. Qin, X. Yang, A. Islam, Y.-B. Cheng, L. Han, *Energy Environ. Sci.* **2015**, *8*, 629-640; bM. Kaltenbrunner, G. Adam, E. D. Glowacki, M. Drack, R. Schwodiauer, L. Leonat, D. H. Apaydin, H. Groiss, M. C. Scharber, M. S. White, N. S. Sariciftci, S. Bauer, *Nat. Mater.* **2015**, *14*, 1032-1039; cP. Docampo, J. M. Ball, M. Darwich, G. E. Eperon, H. J. Snaith, *Nat. Commun.* **2013**, *4*, 2761.
[106]   G. Lu, F. He, S. Pang, H. Yang, D. Chen, J. Chang, Z. Lin, J. Zhang, C. Zhang, *International Journal of Photoenergy* **2017**, *2017*, 1-9.
[107]   N. D. Wu, Y. L. Wu, D. Walter, H. P. Shen, T. Duong, D. Grant, C. Barugkin, X. Fu, J. Peng, T. White, K. Catchpole, K. Weber, *Energy Technol.* **2017**, *5*, 1827-1835.
[108]   D. Wang, M. Wright, N. K. Elumalai, A. Uddin, *Solar Energy Materials and Solar Cells* **2016**, *147*, 255-275.
[109]   C. Wu, X. Zheng, Q. Yang, Y. Yan, M. Sanghadasa, S. Priya, *The Journal of Physical Chemistry C* **2016**, *120*, 26710-26719.
[110]   Z.-K. Tan, Y. Vaynzof, D. Credgington, C. Li, M. T. L. Casford, A. Sepe, S. Huettner, M. Nikolka, F. Paulus, L. Yang, H. Sirringhaus, N. C. Greenham, R. H. Friend, *Advanced Functional Materials* **2014**, *24*, 3051-3058.

Table 1. The expenses

Item	Description	Quantity	Unit Cost (Euro)	Total Cost (Euro)
Visa Processing				
Total costs	For Germany Visa	Many	80	80
Travel Costs				
Flight Costs	Algeria to Germany return ticket	1	400	400
Tlemcen to Algiers	Tlemcen to Algiers to and from	1	40	40
Train to Jena	Frankfurt to Jena	1	70	70
Train From Jena	Jena to Frankfurt	1	30	30
Living Expenses				
Accommodation	For rent + services	6	-	1425
Local transport	For 5 months	5	44	220
Services Required				
Travel and Health insurance	For health from Algeria	1	90	90

Liability Insurance	For Germany	1	60	60
Health Insurance Germany	In Germany	1	70.71	70.71
Student Thoska card	Student registration	1	10	10
			TOTAL	**2495.71**

Equivalent in USD = **USD3,119**

Signatures

Date.....29 8. 2018..............Place..............Jena.....................

Dr. Harald Hoppe...

Student: Chikezie W. Ugokwe..